

Investigating “Lean” Electrodeposited Lithium and Sodium Metal for Hybrid Ion/Metal Carbon Composite Anodes

*David J. Kautz, Lei Tao, Linqin Mu, Muhammad Mominur Rahman, Chunguang Kuai, Zhifeng Zheng, and Feng Lin **

D. J. Kautz, Dr. L. Tao, Dr. L. Mu, M. M. Rahman, Dr. C. Kuai, Prof. F. Lin

Department of Chemistry, Virginia Tech, Blacksburg, VA 24061, USA

Email: fenglin@vt.edu

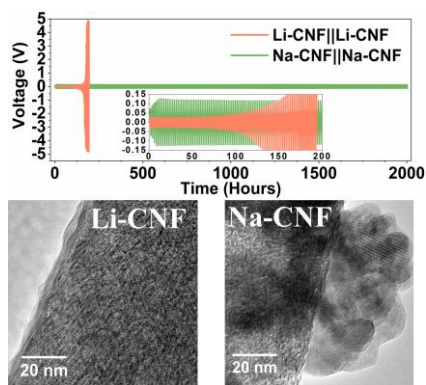
Prof. Z. Zheng

Fujian Engineering and Research Center of Clean and High-valued Technologies for Biomass,

College of Energy, Xiamen University, Xiamen 361102, China

*Corresponding author

Keywords: lithium/sodium batteries, metal composite anode, carbon anode, structural characteristics, intercalation



Abstract

The implementation of alkali metal anodes in practical batteries have been unsuccessful due to major safety concerns related to dendritic growth and thermal runaway. Carbon scaffolds have been utilized as promising host materials in an effort to improve battery safety and performance. Herein, “lean” lithium and sodium composite anodes, using a semi-crystalline carbon nanofiber (CNF) host material with limited surface functionalization, are utilized to investigate the relationship between the structural characteristics of the CNF and lithium/sodium metal. Symmetric testing reveals that the Na-CNF composite anode maintains stable cycling performance, with minimal hysteresis increase over 2000 hours, whereas Li-CNF fails before 200 hours. When paired with layered oxide cathodes ($\text{NaNi}_{0.33}\text{Fe}_{0.3}\text{Mn}_{0.33}\text{Ti}_{0.04}\text{O}_2$ and $\text{LiNi}_{0.6}\text{Mn}_{0.2}\text{Co}_{0.2}\text{O}_2$ for sodium and lithium cells, respectively) and cycled at 1C, the Na-CNF cells maintain 75% capacity retention after 500 cycles, but the Li-CNF cells fail shortly after 140 cycles. The primary factor enabling stable long-term cycling for Na-CNF cells is that Na ion undergoes reversible ion intercalation, whereas Li ion is limited to surface adsorption. The inherent carbon crystallinity is found to govern the interaction between the carbon host and alkali metals and is a primary factor in the sustainability and performance of the metal composite anodes.

Introduction

Batteries with higher energy density are pivotal to support the rapid development of technologies, such as electric vehicles and portable electronics. Conventional graphite anodes will be unable to meet these energy demands with its low theoretical capacity (372 mAh g^{-1}).¹ The reliance on graphite as the commercial anode of choice is unsustainable and will hinder technological innovation due to graphite's impractical volumetric requirements. Throughout the past several decades there has been a determined effort to enable lithium metal as an alternative anode material for secondary batteries due to its high theoretical capacity (3860 mAh g^{-1}), low density (0.534 g cm^{-3}), and low redox potential (-3.040 V vs Standard Hydrogen Electrode, SHE). Lithium metal anode has been utilized in various designs for next-generation batteries such as Li-nickel rich layered oxides, Li-S, and Li-O₂.²⁻⁵ However, lithium metal anodes face many challenges stemming from its high reactivity with electrolyte, unstable solid electrolyte interphase (SEI) formation, and dendrite formation, which collectively results in poor Coulombic efficiency (CE), high hysteresis, and severe safety risks. Various strategies have been employed to improve lithium metal anode performance and reduce safety concerns, including the utilization of electrolyte additives⁶⁻⁸, artificial SEI^{9,10}, and surface modifications.¹¹⁻¹³ More recently, utilizing 3D carbon scaffold current collectors to form metal composite anodes has been a major research effort to contain lithium metal expansion, homogenize local charge density, and limit the lithium metal loading (i.e., "lean" anode).^{1,14,15} To develop a practically viable lithium metal anode, a "lean" composite anode ($<5 \text{ mAh cm}^{-2}$) should be able to sustain long-term cycling and prevent consumption of the limited active material.¹ Multiple previous reports have utilized doping^{16,17}, surface functionalization¹⁸⁻²⁰, and structural modification²¹ of the carbon host to improve the host-guest interaction to increase the lifespan and cycling performance of composite anodes. Although limiting the use of Li metal is critical for practical cells, the "lean" composite anode has been overlooked compared to the composite anodes that use an excess amount of lithium metal.^[17,20,21]

As a potential alternative anode material, sodium metal anode has more recently become a prominent point of interest for secondary battery applications. Sodium metal has a moderately high theoretical capacity (1166 mAh g^{-1}), low redox potential (-2.71 V vs SHE), and moderately low density (0.971 g cm^{-3}). The natural abundance of sodium in the Earth's crust is orders of magnitude higher than that of lithium, making sodium batteries potentially more cost-effective

than lithium. Sodium batteries are mostly attractive for large scale energy grid applications, where size and portability are not the major deciding factors for utilization. However, sodium metal faces many of the same problems that surround lithium metal anodes, such as poor Coulombic efficiency and dendrite formation. Sodium also faces another unique issue. Unlike other alkali metals, sodium has unfavorable interactions with carbon materials.^{25,26} Sodium ions are generally unable to intercalate into graphite as easily as lithium ions. For sodium ions to intercalate into graphite, a large overpotential is required to overcome the energy barriers necessary for ion intercalation, removing graphite as a viable anode material for sodium ion batteries.^{26–28} Hard carbon has been the primary anode material for sodium ions batteries due to the larger (002) d-spacing (3.6–3.9 Å), and Na ions adsorbing onto the surface defects and nanovoids present in hard carbon.^{29–31} Multiple studies have reported and debated about the adsorption-insertion mechanism of Na ions in the hard carbon electrode.^{29,31–34} Sodium metal composite anodes have also begun to be more heavily investigated recently.^{35–37} With the inherent differences in how lithium and sodium interact with carbon materials, it is imperative to ascertain the critical host-guest interactions to improve the synergy, sustainability, and performance of the composite anodes. There have not been many studies on the direct comparison between lithium and sodium metal or on establishing the relationship between the host material, electrochemical characteristics, stability, and performance. However, understanding the key factors that influence the chemical interaction between alkali metals and a carbon host will inform better design of “lean” composite anodes.

Herein, we present a thorough comparison study between lithium and sodium metal composite anodes, under “lean” (3 mAh cm⁻²) conditions, using a semi-crystalline CNF membrane as the host material. We observe major differences between lithium and sodium in terms of the electrodeposition behavior, morphology, and cycling performance. Through kinetic analysis, we determine that the primary ion interaction mechanisms between Na ions and the CNF host are intercalation and adsorption, while Li ions are primarily limited to surface adsorption on the CNF host. When assembled in the full cells, containing layered cathodes, the Na-CNF composite anode can sustain much longer cycle life than the Li-CNF composite anode. The enhanced interaction between Na ions and the crystalline domains of the CNF is shown to be the determining factor for the longevity and sustainability of the sodium composite anode. The crystallinity of the host material is an important factor in the overall performance of the composite anode. Therefore, beyond controlling the surface chemistry of carbon host materials^{17,18,23}, future work on “lean”

composite anodes should also focus on optimizing the host crystallinity for lithium and sodium metal, individually.

Results and Discussion

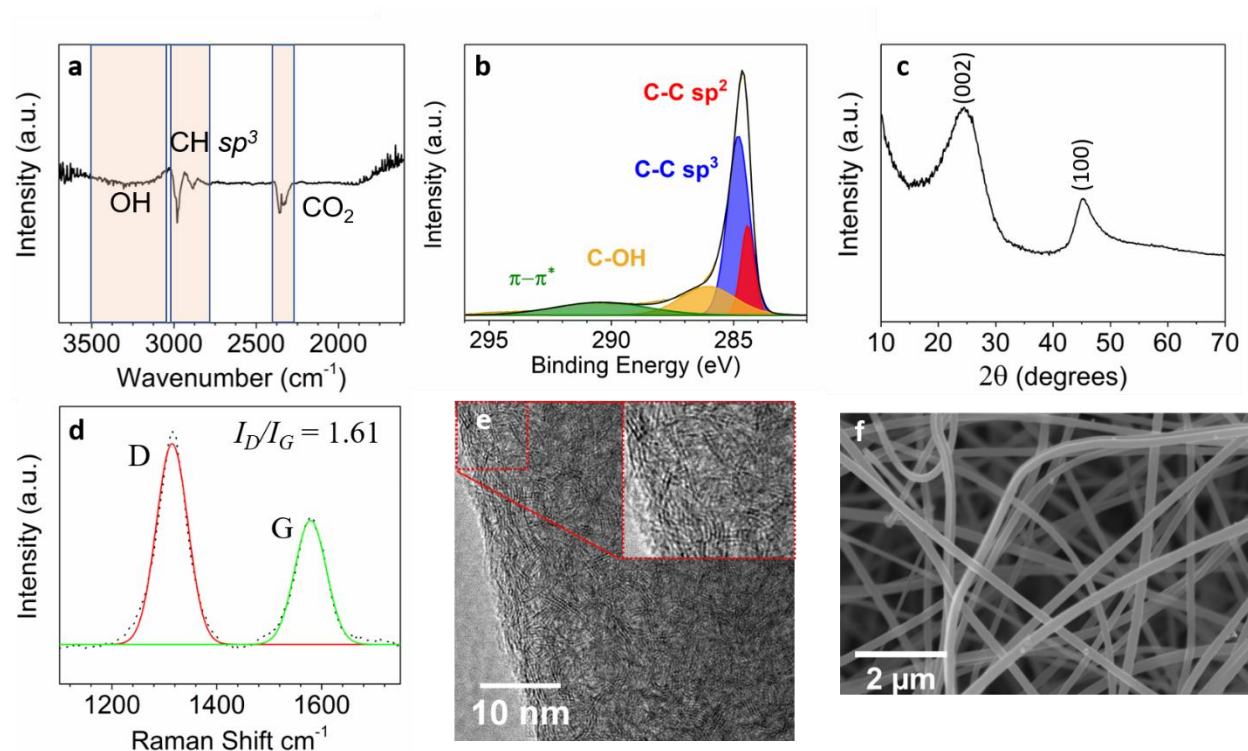


Figure 1) Characterization of the pristine CNF membrane. Surface functionalization analysis of the CNF using **a)** FTIR spectrum and **b)** Deconvoluted XPS C 1s spectra illustrating the limited presence of oxygen related surface functional groups on the CNF. **c)** XRD pattern and **d)** Raman spectra delineating the physical properties and degree of inherent crystallinity throughout the CNF membrane. Representative **e)** TEM image with the inset showing the local crystalline domains and **f)** high magnification SEM image of the pristine CNF membrane.

In-depth characterization analysis was performed to determine the surface functionalization, degree of crystallinity, and structural properties of the CNF host membrane (**Figure 1**). Through the determination of the CNF properties, we will be able to better understand the chemical interaction between alkali metals and the CNF host. Fourier transformed infrared spectroscopy (FTIR) showed minimal surface functionalization on the CNF membrane, with a weak -OH band and adsorbed CO₂ to the surface of the CNF (Figure 1a). C 1s X-ray photoelectron spectroscopy (XPS), confirmed the limited presence of oxygenated species. The sp² crystalline π - π^* satellite

peaks observed (~ 291 eV)^{37,38}, establishes the presence of ordered crystalline layers of the CNF (Figure 1b). The O 1s further confirmed that -OH is the only oxygen containing functional group present on the surface of the CNF (Figure S1) and compositional analysis from the XPS analysis shows that the CNF contains 97.6% C and 2.4% O (H is not probed). Through X-ray diffraction (XRD), two broad peaks at (002) and (100) are observed (Figure 1c). The d_{002} peak at 24.8° corresponds to the diffraction of a graphitic crystalline lattice with a calculated d-spacing of 3.59 Å using the Bragg's law, which is within the range between hard carbon materials and pure graphite d_{002} at 3.35 Å.^{29,39} The degree of crystallinity was determined through Raman spectroscopy (Figure 1d). The two narrow peaks with a clear separation between the D band ($1200-1500\text{ cm}^{-1}$) and the G band ($1500-1700\text{ cm}^{-1}$), reveal the presence of well-developed hexagonal carbon structures in the CNF.⁴⁰ The peak area I_D/I_G ratio is 1.61, indicating a mostly amorphous material with some degree of crystallinity. Through transmission electron microscopy (TEM), the crystalline layers are observed to be, on average, 3-5 layers thick with a pattern of turbostratic crystalline ribbons that thread throughout the CNF structure (Figure 1e). The surface of the CNF to be generally smooth through scanning electron microscopy (SEM) imaging (Figure 1f). The Brunauer–Emmett–Teller specific surface area was calculated, utilizing the N₂ gas adsorption/desorption isotherms, to be $18.8\text{ m}^2\text{ g}^{-1}$ (Figure S2). From the structural information gathered through these characterization analyses, the CNF can be described to have a semi-crystalline composition and structure. The determination of the inherent crystallinity and surface functionalization will give insight into understanding the electrochemical behavior of Li/Na-CNF composite anodes.

The surface functionalization and graphitization content determine the lithio/sodiophilicity of the substrate and the deposition characteristics of lithium and sodium metal.^{18,41} Through the utilization of electrodeposition, the morphology of the electrodeposited lithium and sodium metal as well as the interaction between lithium/sodium and the CNF host is investigated. We use a metal deposition of 3 mAh cm^{-2} areal capacity (lithium or sodium metal) to test the feasibility of utilizing a “lean” anode for practical cycling conditions.¹ The deposition profiles presented for the metal-carbon nanofiber composites (M-CNF) are an average of three separate electrodepositions, with red error bars included (**Figure 2a,d**). In the Li-CNF electrodeposition profile, the voltage immediately drops to below 0 V, beginning the nucleation of the lithium metal phase, with a nucleation overpotential of 17 mV (Figure 2a). Despite the CNF having crystalline domains, there

is no direct observation of the voltage plateaus indicative of the LiC_y formation during electrodeposition, that is typically observed $\sim 0 - 0.2$ V (Figure 2a).^{27,42,43} However, when performing electrodeposition of lithium metal on graphite, the prominent voltage plateaus of LiC_y and LiC_6 are observed (Figure S3a). Lithium metal nucleation and plating is shown to occur earlier for the CNF, compared to graphite. The quick voltage drop to 0 V and lack of distinctive intercalation plateaus for Li-CNF (Figure 2a) implies that the semi-crystalline CNF does not readily undergo Li ion intercalation, unlike graphite. The Li nucleation potential on graphite is 5 mV, which is smaller than that observed for the CNF (17 mV) (Figure S3a). The crystalline domains in graphite are much more ordered than those in the CNF, which allows for enhanced electron transfer kinetics and overlap of the alkali metal ion and the π bonds between graphitic layers.²⁷

The Na electrodeposition on the CNF shows a prominent distinction in the deposition behavior (Figure 2d). Two small bumps are observed at 0.38 V and 0.33 V due to initial side reactions, decomposition of the electrolyte, and SEI formation.^{29,39,44} Similar to the Li-graphite profile (Figure S3a), the nucleation peak is observed further into the electrodeposition process, occurring at 1.25 mAh cm^{-2} , with a nucleation overpotential of 5 mV. The sloping region before the Na metal nucleation can be attributed to the Na ion adsorption into the defect sites or nanovoids present in the CNF.^{32,39} The different electrodeposition profiles may signify the contrasting interaction that the Li and Na have with the CNF host.

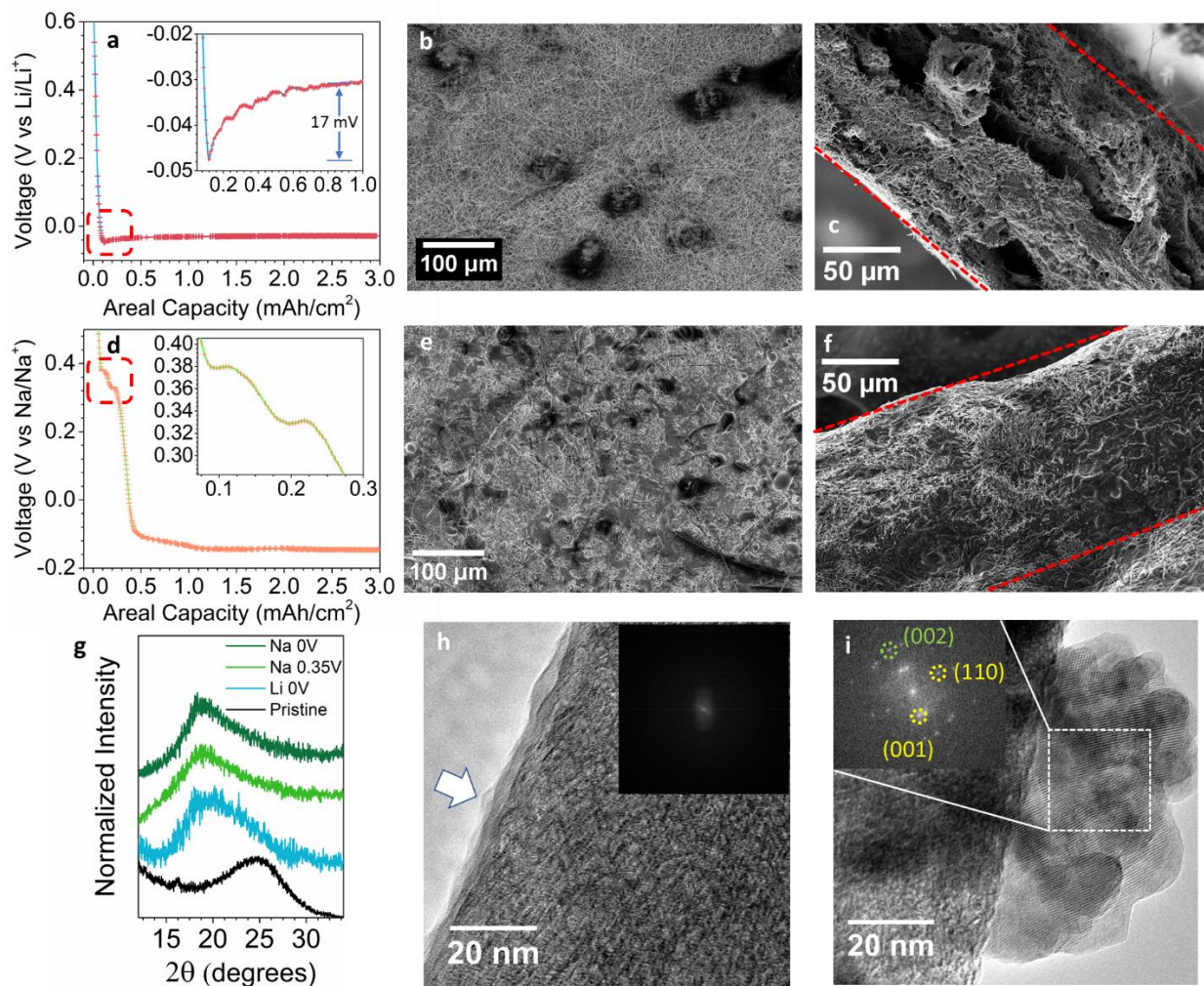


Figure 2) **a)** Li electrodeposition profile on the fresh CNF host (Li-CNF). **b,c)** SEM images of the top side and cross section of Li-CNF. **d)** Na electrodeposition profile on the fresh CNF host (Li-CNF) **e,f)** SEM images of the top side and cross section of Na-CNF. **g)** XRD pattern of the pristine CNF and after discharging to different voltages. TEM images of **h)** Li-CNF and **i)** Na-CNF after 3 mAh cm⁻² metal deposition with inserts of FFT dot patterns of the surface compounds on the electrodes. The deposition profiles presented for the M-CNFs are an average of three separate electrodepositions, with red error bars included in **a** and **d**.

After electrodeposition, XRD was utilized to investigate the occurrence of lithium or sodium ion intercalation into the CNF. Although a prominent intercalation plateau is not observed for the Li electrodeposition on the CNF, a peak shift from 24.8° to 20.0° is observed in the XRD pattern. A d_{002} expansion of 0.85 Å is calculated, slightly larger than the Li⁺ ionic radius of 0.76

Å, indicating the occurrence of Li ion intercalation. For the Na electrodeposition on the CNF, a larger peak shift to 18.6° is observed at both 0.35 V and 0 V (Figure 2), correlating to a d_{002} expansion of 1.18 Å, similar to the Na^+ ionic radius of 1.02 Å.^{27,45}

SEM was taken for the composite anodes after electrodeposition to examine Li/Na metal plating behavior. The Li-CNF composite anode was found to have heterogenous plating of lithium metal scattered throughout the surface on the topside of the CNF (Figure 2b). Lithium metal preferred to gather in large clusters and did not envelope the CNF as a coating layer. With the high carbon and low oxygen content and lack of surface functionalization, the CNF host was found to be lithiophobic and did not undergo homogenous lithium plating throughout the electrode.¹⁸ The bottom side of the electrode was also inspected to view the penetration of Li metal throughout the CNF membrane. Smaller lithium metal clusters were heterogeneously plated along the bottom of the CNF (Figure S4a,b). Metal clusters were observed in the cross section as well (Figure 2c). In summary, lithium metal does not homogeneously plate within the CNF membrane. Instead, there is a random distribution of metal clusters throughout the Li-CNF composite anode. A photograph of the composite anode macroscopically shows that the lithium metal distribution is heterogenous, growing in large web-like patterns and in scattered metal clusters (Figure S4d). In contrast, we observe a homogenous distribution of sodium metal throughout the CNF membrane. The topside of the Na-CNF anode (Figure 2e) shows a dense coating of sodium deposition, fully covering the CNF surface. The cross-section SEM image also shows that sodium metal is homogeneously coated throughout the CNF (Figure 2f). The bottom side of the composite anode also exhibits dense and relatively homogenous sodium metal coating (Figure S5a). The pre-sodiation of the CNF through Na ion intercalation and adsorption during the early stage of electrodeposition (Figure 2d) likely increases the nucleation sites for sodium metal deposition.⁴⁶ The increased number of nucleation sites enhances the sodiophilicity of the CNF and improves the chemical affinity between sodium metal and the host material, resulting in the homogenous coating of sodium metal on the CNF membrane.⁴⁶ The photograph of the Na-CNF surface also shows a homogeneous distribution of sodium deposition on the CNF membrane (Figure S5d).

TEM was performed after electrodeposition for the M-CNF composite anodes to ascertain the distinct plating behavior of both alkali metals. As expected, no distinctive coating of Li metal on the CNF surface was observed (Figure 2h). A thin layer is observed on the surface of the CNF

(indicated by the arrow in Figure 2h), which may be a thin passivation layer resulting from the electrolyte decomposition. No pattern was observed from the fast Fourier transform (FFT) analysis of the TEM image, suggesting that no detectable amount of crystalline compounds or lithium metal is present on the surface of the Li-CNF sample. Furthermore, the individual carbon fibers are free of noticeable deposition on the surface (Figure S6a-c) due to the weak affinity between lithium and the CNF, which is consistent with the above SEM results. In sharp contrast, after sodium electrodeposition, clear deposition has formed throughout the surface of multiple fibers (Figure S6d-f). Lattice fringes are observed in higher magnification of the Na-CNF. The FFT patterns detected are reminiscent of Na_2CO_3 crystal planes (Figure 2i). The presence of Na_2CO_3 is attributable to either SEI or the transformation of sodium metal during the TEM sample handling.

The SEI composition was investigated through XPS analysis of the composite anodes after deposition (Figure S7). For C 1s, O 1s, and Li/Na 1s, a stronger peak intensity for Na_2CO_3 relative to Li_2CO_3 is observed. This finding is consistent with the large presence of Na_2CO_3 on the surface of the Na-CNF fibers from TEM analysis (Figure 2i). In the F 1s and Li 1s spectra, LiF is more abundant than Li_2CO_3 . On the other hand, NaF is shown to have low intensity in the F 1s and to be less abundant than Na_2CO_3 in the Na 1s spectrum. The increased amount of inorganic fluorinated species can improve the protective and ionic qualities in the SEI of the electrodeposited metals.^{47–49} Even with the addition of FEC to the sodium electrolyte, the formation of Na_2CO_3 during the electrolyte decomposition is greater than NaF. The prominent CO_3^{2-} peaks in the XPS spectra also confirm the increased amount of side reactions with the electrolyte during Na metal electrodeposition, inactivating a portion of the electrodeposited metal.

To further investigate the metal-host interaction, M-CNF symmetric cells were designed to establish the relationship between performance and the characteristics of the CNF host. Symmetric cells were cycled with a current density of 0.5 mA cm^{-2} for a 0.5 mAh cm^{-2} areal capacity. In these symmetric cells, both electrodes were loaded with “lean” metal anode (3 mAh cm^{-2}) using the same electrodeposition process prior to the symmetric cell assembly. The Li-CNF symmetric cell sustained stable cycles for 160 hours before the cell overpotential gradually began to increase, with the cell shorting at 195 hours (**Figure 3a**). The Na-CNF symmetric cell, however, sustained stable cycling for over 2,000 hours, with minimal overpotential increase. In the zoomed-in profiles for selected cycles (Figure 3b-e), we observed the transformation of the voltage profile

for the Li-CNF symmetric cell over the cycle life, while the Na-CNF symmetric cell remains fairly stable over the 2,000 hours. The Li-CNF symmetric cell has an initial overpotential of 30 mV, which is comparatively lower than that of the 75 mV of the Na-CNF symmetric cell. However, over time the Li-CNF symmetric cell fails to prevent side reactions with the electrolyte, causing the rapid consumption of lithium metal.¹⁴ An unforeseen observation for the Na-CNF symmetric cell is that within the first 10 cycles, the primary cycling mechanism changed from metal stripping/plating to intercalation/surface adsorption (Figure S8).²⁹ The voltage profile during cycling also reflects this change if we compare the first cycle to the 50th cycle (Figure 3b,c). The relatively flat voltage curve that is associated with metal stripping/plating changes to a sloping profile that is maintained throughout the rest of its cycle life (Figure 3b-e). Such a change from stripping/plating to intercalation/surface adsorption may protect Na ions from being consumed by the electrolyte side reactions, thus allowing the Na-CNF symmetric cell to have a long cycle life.

The alkali metals were electrodeposited onto copper foil discs and cycled as M-Cu symmetric cells and M-CNF||M-Cu cells to determine the active role of the CNF host on the cycling performance of the composite anodes. Li-Cu symmetric cells only sustained 60 hours of stable cycling before succumbing to lithium metal consumption and shorting (Figure 3f). The addition of the CNF composite anode in the Li-Cu||Li-CNF cell prolongs the lifespan of the cell approximately by 30 hours, but still succumbed to active metal depletion faster than the Li-CNF symmetric cell. As seen in the inset of Figure 3f, the Li-CNF symmetric cell has the lowest stripping/plating overpotential. The overlap between Li/Na p-orbitals and the π bond network of the crystalline domains of the CNF improves electron transfer throughout the electrode, lowering the overpotential needed for stripping/plating.²⁷ The cells that incorporate Na-Cu, however, show that the electrodeposited sodium metal fails to cycle more than 1-2 cycles before a sudden voltage increase, resulting in the cell shorting (Figure 3g). Even the inclusion of the Na-CNF anode failed to sustain stable cycling for more than 2 cycles when paired with Na-Cu (Figure 3g). The electrodeposited sodium metal on the Cu foil undergoes rapid consumption and reactions with the electrolyte, producing inactive sodium on the substrate. The Na-CNF symmetric cell improves the cycle life by a factor of over 2,000, which is primarily due to the change in Na-CNF interaction mechanism from plating/stripping to intercalation of Na ion into the crystalline domains of the CNF and adsorption onto the CNF surface.

The difference in the electrochemical stability of Li-CNF and Na-CNF composite anodes in Figures 3f and 3g led us to test the sustainability of the limited amount of electrodeposited metal by using a M||CNF configuration and performing plating/stripping cycles for an areal capacity 0.5 mAh cm^{-2} of Li/Na metal onto the pristine CNF (Figure 3h,i). For the Li||CNF cell, over the period of 35 cycles, we observe high capacity reversibility and a lower hysteresis. For the Na||CNF cell, a much lower capacity reversibility is observed, and the capacity recovered from the first stripping cycle is approximately 60% of the plated capacity. The increase in voltage hysteresis over the 35 cycles is more drastic than the Li||CNF cell. With a smaller amount of metal deposited, we were able to more accurately investigate the electrochemical behavior and stability of the metal itself. The electrodeposited lithium metal, as we see in our case, is less reactive with the electrolyte and has a higher degree of metal sustainability during the plating/stripping cycles, compared with electrodeposited sodium metal. Collectively, we further confirm, through Figures 3f-i, that the primary factor that the Na-CNF symmetric cells are able to sustain over 2000 hours (Figure 3a), without significant increase in polarization, is due to the intercalation and adsorption that Na ions undergo with the semi-crystalline lattice of the CNF, rather than the stability of the sodium metal itself.

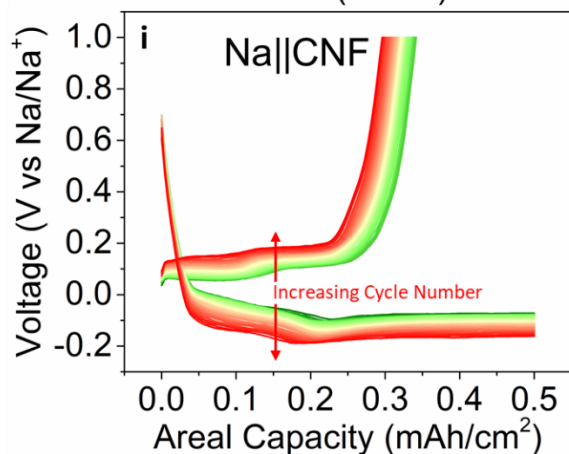
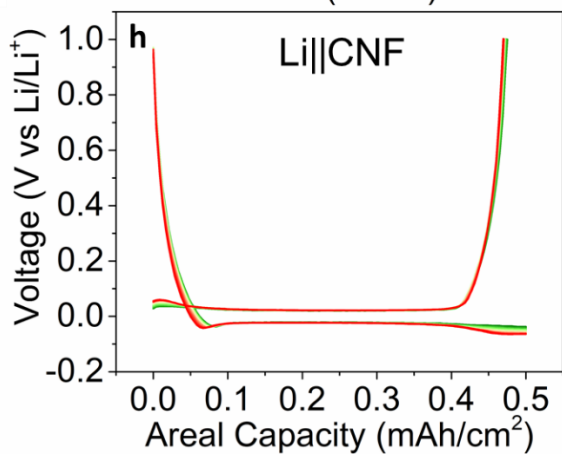
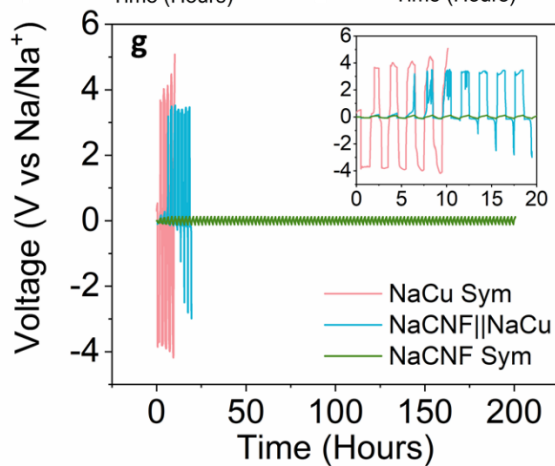
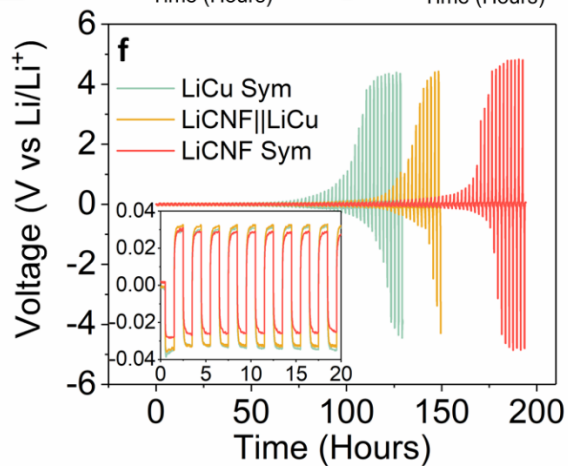
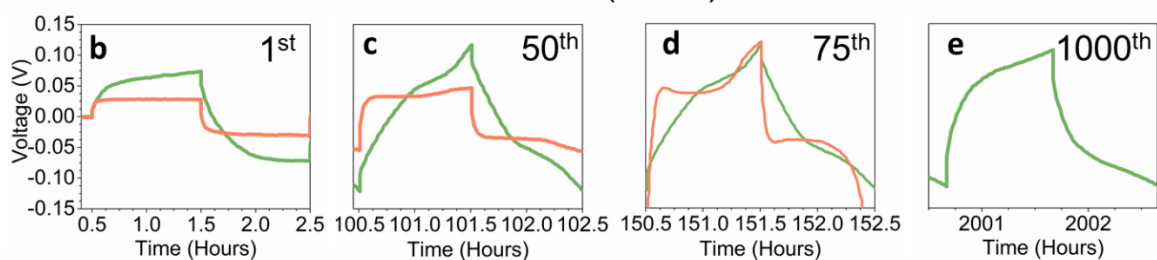
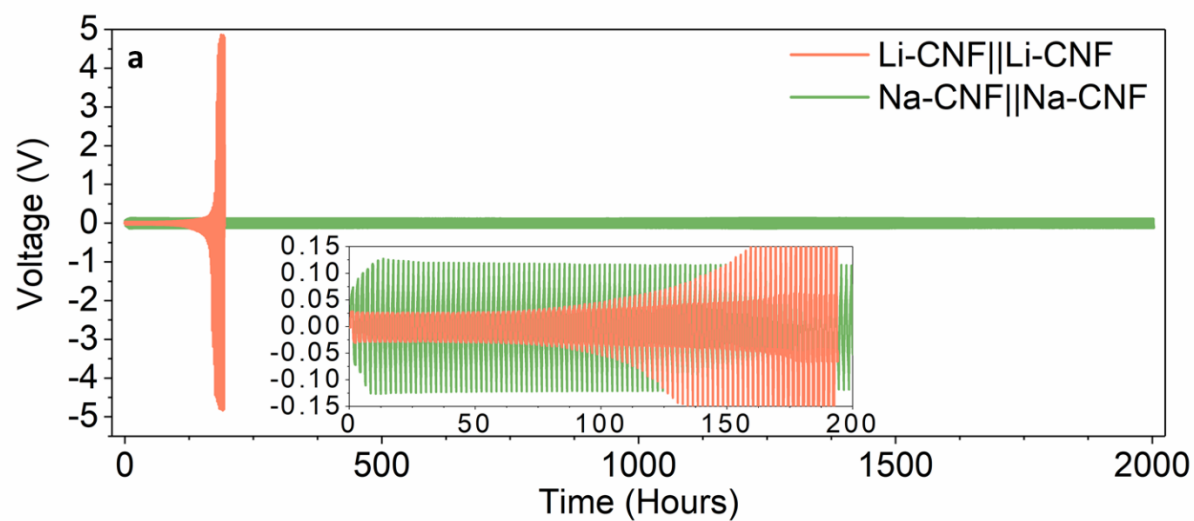


Figure 3) Electrochemical performance evaluation of Li-CNF and Na-CNF composite anodes. **a)** M-CNF||M-CNF symmetric cell performance for Li-CNF and Na-CNF anodes cycled at 0.5 mA cm⁻² for a 0.5 mAh cm⁻² areal capacity. The starting M loading in M-CNF is 3 mAh cm⁻², which was electroplated in the M||CNF cell and collected for the symmetric cells. Insets of M-CNF symmetric cell cycling for the **b)** 1st, **c)** 50th, **d)** 75th, and **e)** 1000th cycles. Comparison between M-Cu||M-Cu, Mn-Cu||M-CNF, and M-CNF||M-CNF symmetric cycling performance for **f)** lithium and **g)** sodium. Plating/stripping of M||CNF with a current density of 0.5 mA cm⁻² and a cutoff areal capacity of 0.5 mAh cm⁻² over 35 cycles to test the stability of limited electrodeposited **h)** lithium and **i)** sodium metal. Cells for electrochemical testing were cycled at 22 °C.

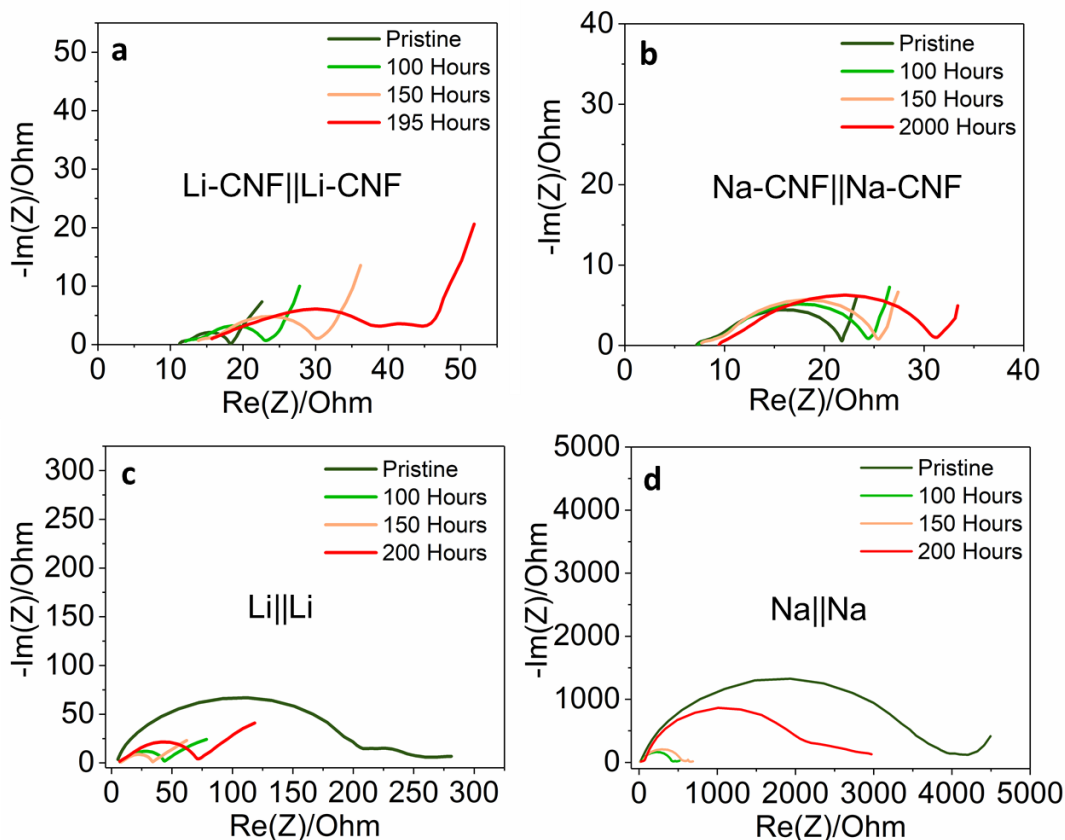


Figure 4) Electrochemical impedance spectroscopy Nyquist plots of **a)** Li-CNF||Li-CNF, **b)** Na-CNF||Na-CNF, **c)** Li||Li metal, and **d)** Na||Na metal symmetric cells after stripping/plating cycles with a current density of 0.5 mA cm⁻² and cutoff areal capacity of 0.5 mAh cm⁻².

After different stages of cycling, for the M-CNF||M-CNF and M||M symmetric cells, electrochemical impedance spectroscopy (EIS) was utilized to correlate the change in the cell

internal resistance with the change in the cell overpotential during cycling, previously shown in Figure 3a. The cells were measured after full stripping/plating cycles at OCV to retain a nominal 0% state of charge. The pristine M-CNF||M-CNF symmetric cells show much smaller impedance than the pristine M||M symmetric cells. This observation may be explained by the fact that SEI layers are formed on the composite anodes during the electrodeposition to prepare M-CNF electrodes, which may drastically improve the initial electrode-electrolyte interface. The pristine Li-CNF and Na-CNF symmetric cells are similar in their impedance values, with the main distinction that Na-CNF has a slightly larger semi-circle related to higher charge transfer resistance, and Li-CNF has a more prominent tail end slope attributed to the solid-state mass transfer resistance in the active material.⁵⁰ With increasing cycle time, the impedance of the Li-CNF symmetric cell increases more rapidly (**Figure 4a**), matching the increase in overpotential during cycling (Figure 3a). The formation of second semi-circle corresponds to the depletion of active lithium metal and increase in SEI layer thickness (Figure 4a).⁵⁰ While the Na-CNF cell starts off with a slightly higher impedance, it maintains considerable stability over 2,000 hours. The slow increase and stability of the impedance values are consistent with the highly stable cycling performance and overpotential in Figure 3a. The impedance only increased slightly after 2000 hours of cycling, which is likely attributed to the highly stable SEI and reversibility of Na⁺ intercalation/de-intercalation within the semi-crystalline CNF.

The pristine full metal symmetric cells have large initial impedance due to high interfacial resistance without the presence of a formed SEI on the metal surface to improve electrode-electrolyte interaction (Figures 4c,d). After cycling for 100 hours, the SEI is fully formed and the impedance for both lithium and sodium metal symmetric cells were significantly reduced. Over 200 hours, the impedance values gradually increase for lithium (Figure 4c). However, more notable impedance growth is observed for the sodium symmetric cell after cell shortage (Figure 4d and Figure S9). The SEI of the full metal symmetric cells are unstable and unable to accommodate the volume fluctuation of the constant heterogeneous plating/stripping cycles, which may lead to the formation of cracks in the SEI and increasing amounts of side reactions between the electrolyte and freshly exposed metal surfaces.^{51,52} Therefore, compared to the full metal anodes, the composite anodes have a much lower impedance due to the enhanced stability and local charge homogeneity potentially benefited from the π - π network in the CNF.⁵³

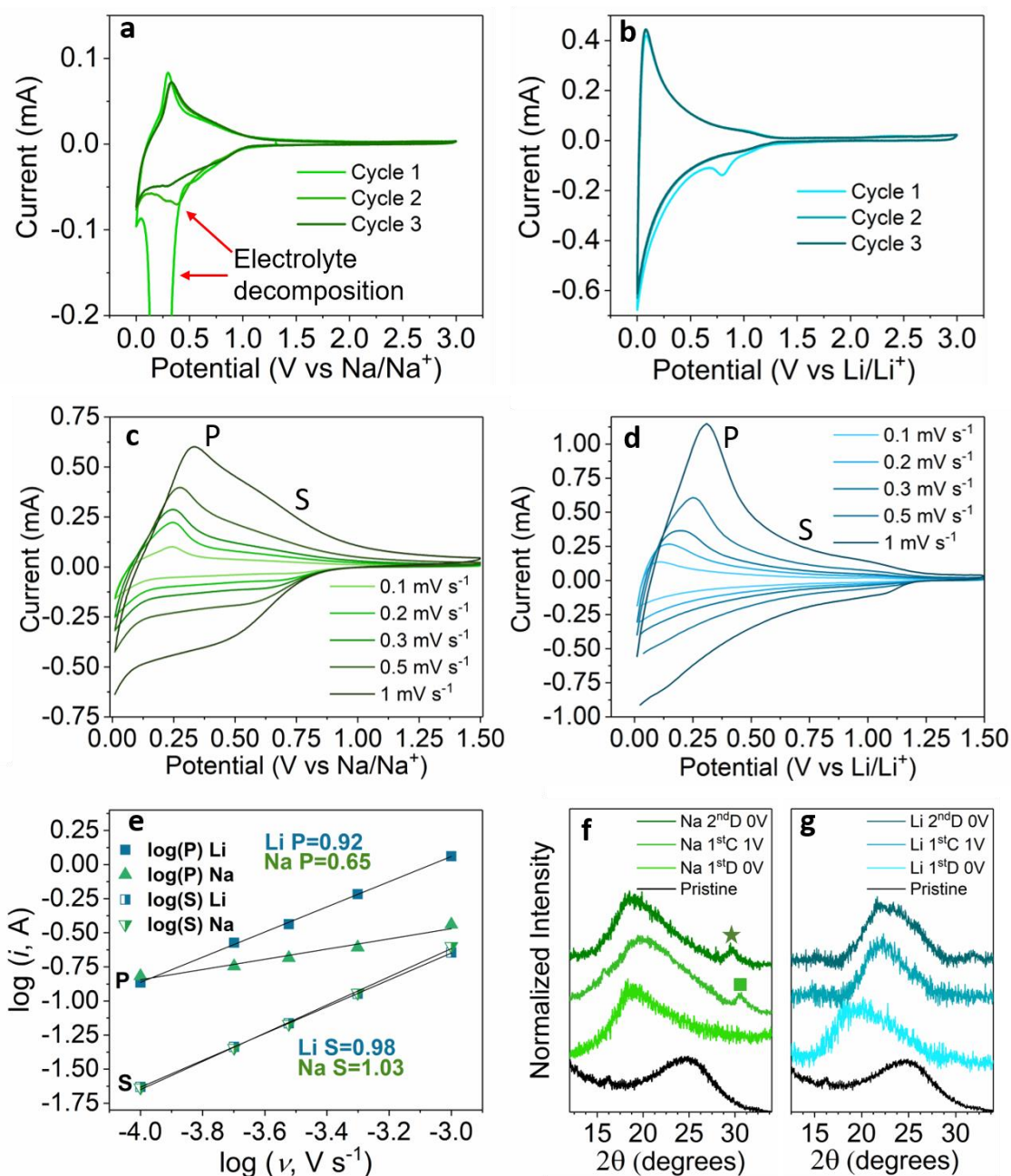


Figure 5) Electrochemical investigation of the interaction between Na/Li ion and the pristine CNF. Cyclic voltammetry (CV) of **a)** Na||CNF and **b)** Li||CNF at a scan rate of 0.1 mV s^{-1} and a voltage range of 0.01 – 3 V. CV at different scan rates for **c)** Na and **d)** Li. **e)** The corresponding correlation between the scan rate and peak current at low potential (peak (P), $\sim 0.1 \text{ V}$) and at high potential (slope (S), $\sim 0.75 \text{ V}$). XRD of the CNF anode after charge/discharge for **f)** Na and **g)** Li. The peaks marked with the star and box are attributed to sodium metal formation and electrolyte decomposition, respectively.

Through symmetric electrochemical cycling and EIS analysis, a disparity in the performance and host-guest interactions of lithium and sodium metal composite anodes was observed. Although we observed carbon d_{002} expansion after lithium and sodium electrodeposition, the sodium composite anode has exhibited superior electrochemical stability and performance. Further electrochemical diagnostics was performed to probe the chemical interaction between the alkali metal and the CNF. To determine the degree and reversibility of the Li/Na ion interaction with the pristine CNF, cyclic voltammetry (CV) was utilized with a scan rate of 0.1 mV s^{-1} between 0.01-3 V (**Figure 5a,b**). Magnified profiles at a lower potential window are shown in Figure S10 (Supporting Information). During the first reduction process for the Na||CNF cell, the two reduction peaks $\sim 0.5 \text{ V}$ and 0.25 V (indicated by the arrows in Figure 5a and Figure S10a) are associated with the electrolyte decomposition and SEI formation. Another small reductive peak below 0.1 V is attributed to Na^+ intercalation into carbon crystalline domains.²⁹ On the subsequent oxidation process, the small oxidative peak observed is related to the de-intercalation of Na^+ from the crystalline domain.²⁹ A new reductive peak is observed during the second reductive process $\sim 0.38 \text{ V}$, matching the plateaus observed during electrodeposition (Figure 2d). During the third cycle, the reductive peak at 0.38 V becomes much less prominent, indicating subdued side reactions of the electrolyte. For the Li||CNF cell, a small reduction peak $\sim 0.8 \text{ V}$ on the first discharge cycle shows that the initial side reactions for the SEI formation are less severe compared to what we observe in the Na||CNF cell. The Li||CNF cell has prominent oxidation/reduction peaks $\sim 0.1 \text{ V}$ and are highly stable over the three CV cycles, which is related to Li ion adsorption onto the CNF surface.⁴⁵

The kinetic analysis of CV curves at different scan rates has been proven to be a useful method for determine the mechanism of the host-ion interactions.^{29,54} By using a curve fitting equation $i = av^b$ we can understand the relation between scan rate (v) and the measured peak current (i). The b-value is ascertained from the slope of $\log(v)$ and $\log(i)$. A b-value close to 0.5 is indicative of a more diffusion-controlled reaction, such as intercalation, and a b-value of 1 indicates fast kinetics and primarily surface mass transport such as surface adsorption.^{29,54} The scan rates used range from 0.1 mV s^{-1} to 1 mV s^{-1} . The sharp peak at $\sim 0.1 \text{ V}$ corresponds to the charge/discharge plateau region below 0.1 V labeled (P) and $\sim 0.75 \text{ V}$ for the slope region labeled (S) (Figures 5c-d). The fitted b-values for the P region for lithium is 0.922 and 0.653 for sodium, with an R^2 of 0.99 and 0.97, respectively, (Figure 5e). The b-values indicate that at low voltage

the primary ion-host interaction for lithium is surface adsorption and for sodium is bulk intercalation into the crystalline domain of the CNF. For the S region, i.e., at higher voltage, the b-value for lithium is 0.98 and sodium is 1.03, with an R^2 of 0.99 for both lithium and sodium, representing that both metal ions undergo surface adsorption with the CNF. These results show that Li-CNF interaction is primarily surface adsorption, whereas Na^+ undergoes both surface adsorption and intercalation into the CNF crystalline domains.

The degree and reversibility of ion intercalation was then tested by cycling M||CNF cells at a low current density of 0.05 mA cm^{-2} between 0.01-1 V (Figure S11) followed by *ex-situ* XRD of the cycled CNF anodes (Figure 5f,g). When cycled at the lower current density, a considerable change in the discharge voltage profile is observed for both Li||CNF and Na||CNF cells, compared to the electrodeposition profiles in Figure 2. During the first discharge for the Na||CNF cell, a long plateau is observed (Figure S11b). The plateau is related to a significant amount of side reactions and SEI formation, similar to the large current peak in the initial CV reduction process (Figure 5a). On the subsequent charging cycle, a significant irreversible capacity is observed, also indicating extensive side reactions from the SEI formation during the first discharge. The second discharge shows similar capacity to the charging step and better Coulombic efficiency. The first discharge for Li||CNF has a large sloping discharge curve (Figure S11a), compared to the quick voltage drop to 0 V observed during electrodeposition (Figure 2a). Overall, compared to the Na||CNF cell, the Li||CNF cell has less severe initial electrolyte side reactions, better capacity reversibility, and higher capacity, similar to other reports investigating lithium and sodium ion performance with carbonaceous anodes.^{26,27,55} The sloping profiles for the Li||CNF cell during discharge, even at a low current density, further support that the surface adsorption is the predominant interaction mechanism between Li ion and the CNF. This result is consistent with the CV kinetics analysis (Figure 5e).

The cycled CNF anodes were retrieved and *ex-situ* XRD was performed to observe the reversibility of Na ion and Li ion intercalation/deintercalation within the crystalline domain. The d_{002} peak exhibits a left shift in the XRD pattern, corresponding to an interlayer d_{002} expansion by 1.16 \AA , after the Na||CNF cell is discharged in the first cycle (Figure 5h). After the subsequent charging step, a slight right shift in the XRD pattern is observed, depicting incomplete removal of Na^+ from the lattice and the formation of a new peak $\sim 31^\circ$, reported to be related to the

decomposition of the electrolyte.²⁹ The XRD pattern after the second discharge highlights the reversibility of the ion intercalation with the d_{002} peak shifting back to an overlapping position, consistent with the pattern after the first discharge. A new peak developed after the second discharge at 29.8° related to formation of sodium metal.³⁹ A noticeable difference is shown in the XRD patterns between sodium and lithium after cycling (Figure 5h,i). We observe a greater degree of a right shift for the corresponding d_{002} peak after the Li||CNF cell is charged, showing that Li ion has a greater extent of deintercalation. However, in the second discharge cycle, there is no discernable shift in the d_{002} peak, which indicates that Li ion cannot be re-intercalated into the crystalline domain of the CNF.

In summary, the electrochemical and structural analyses highlight the different interaction mechanisms of Li ion and Na ion with the CNF host. The primary interaction mechanism for Li ion is the surface adsorption, whereas Na ion has a combined adsorption-intercalation mechanism. The intercalation of Na ion into the crystalline domain promotes the long cycle life of the Na-CNF composite anode (Figure 3a). The CNF host may act as a “scavenger” to protect the intercalated Na ions from being consumed by side reactions with the electrolyte. When the electrodeposited metallic sodium is depleted, the Na-CNF composite anode can still continue stable cycling because of the availability of the intercalation mechanism. However, the Li-CNF composite anode begins to fail rapidly after undergoing lithium metal depletion.

The “lean” metal composite anodes were then paired with $\text{LiNi}_{0.6}\text{Mn}_{0.2}\text{Co}_{0.2}\text{O}_2$ (NMC 622) and $\text{NaNi}_{0.33}\text{Fe}_{0.3}\text{Mn}_{0.33}\text{Ti}_{0.04}\text{O}_2$ (NFM 333) cathodes, respectively, to test the practical viability of the composite anodes in full cells. The cells containing NMC were cycled between 2.5–4.5 V vs. Li/Li^+ and the cells containing NFM 333 were cycled between 2.0–4.0 V vs. Na/Na^+ . These are common cutoff voltages used for these materials in the literature.^{56–59} The typical galvanostatic discharge profiles are shown in Figures S11 (Supporting Information). The initial discharge capacities in both cells match well with the values reported in the literature.^{56–59} Initially, similar cycling performance is observed for both full cells (**Figure 6a**). At 140 cycles, the Li-CNF full cell begins to undergo rapid cell failure, quickly depleting the limited electrodeposited lithium metal. The Li-CNF full cell retains ~10% capacity for the rest of the long-term cycles. In contrast, Na-CNF maintains a 75% retention after 500 cycles, which is competitive to the sodium foil cell (80%), and slightly higher than the Na-HC composite anode (73%) after 500 cycles (Figure S13a).

To determine whether the high upper cutoff voltage (4.5 V vs. Li/Li⁺) plays a role in accelerating the consumption of Li metal in the Li-CNF composite anode, the upper cutoff voltage was lowered to 4.3 V (Figure S14a). The % capacity retention profile is similar to the full cell with an upper cutoff voltage of 4.5 V. These results indicate that the upper cutoff voltage or the amount of cathode capacity that is cycled, does not play a significant role in the lifespan of the cell containing the Li-CNF composite anode. At a 2C rate we observed that the capacity fade of the Li-CNF full cell is more severe (Figure 6d). The capacity retention of the Na-CNF full cell at 2C increases to 87.5% after 500 cycles and outperforms the cell containing the pure sodium metal foil anode (80%) (Figure S13c).

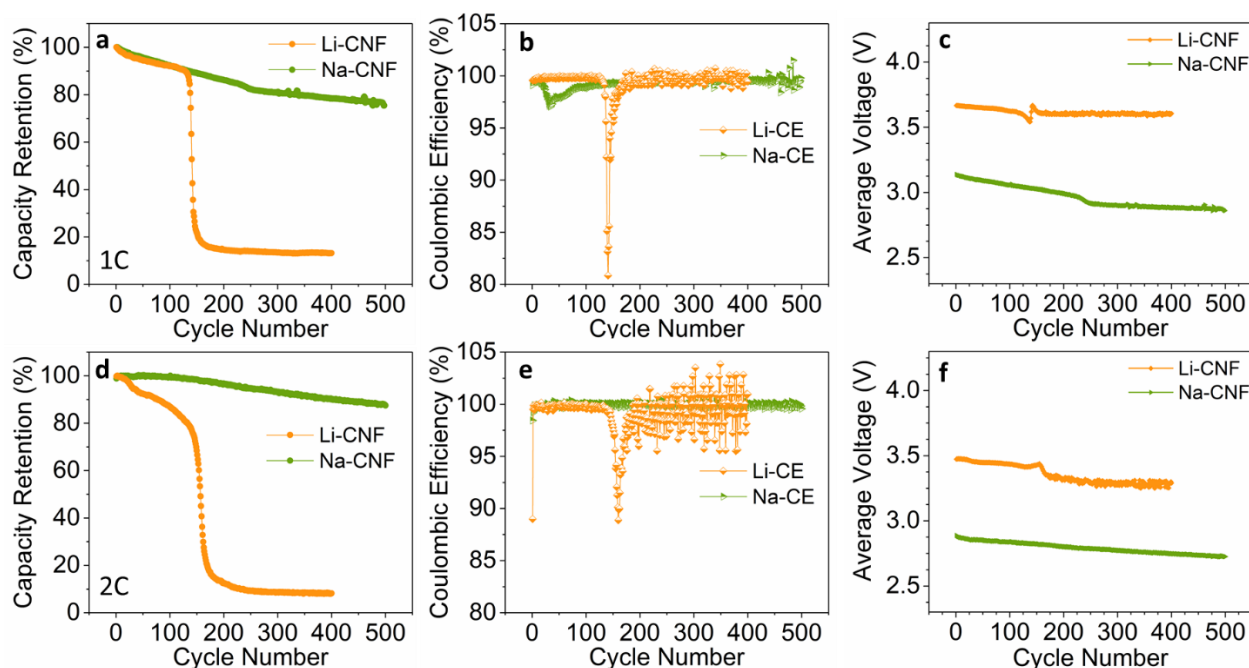


Figure 6) Electrochemical performance of the full cells containing the Li-CNF and Na-CNF composite anodes. The configurations are $\text{LiNi}_{0.6}\text{Mn}_{0.2}\text{Co}_{0.2}\text{O}_2\|\text{Li-CNF}$ and $\text{Na}_{0.96}\text{Ni}_{0.33}\text{Fe}_{0.33}\text{Mn}_{0.33}\text{Ti}_{0.04}\text{O}_2\|\text{Na-CNF}$. The voltage window of the lithium full cell is 2.5 – 4.5 V vs. Li/Li⁺ and the voltage window of the sodium full cell is 2.0 – 4.0 V vs. Na/Na⁺. The cells are cycled at 1C (**a-c**), and 2C (**d-f**). (**a,d**) Percent capacity retention, (**b,e**) Coulombic efficiency, and (**c,f**) average voltage. Cells for electrochemical testing were cycled at 22 °C. C rate for Li and Na full cells is the time required to fully charge/discharge cell relative to a specific current density.

Both Li- and Na-CNF full cells maintain a ~99.5-99.9% CE during their stable cycling periods. When the Li-CNF full cell begins the state of rapid cell failure, a decrease in the CE is observed, dropping rapidly to 80% for 1C and 89% for 2C before developing an erratic and unstable behavior. The CE for Na-CNF remains fairly stable for the entirety of the 500 cycles (Figure 6b). The average voltage delivered by the composite anode full cells shows good stability and consistency, comparable with the alkali metal half cells (Figures 6c, f and Figure S15). During the stable cycling phase for all Li-CNF full cells, there was a minimal decrease in the average voltage. Similar to the trend observed for the CE in Figure 6b, a sharp fluctuation in the average voltage signaled the stage of rapid cell failure, followed by unstable cycling behavior in subsequent cycles. The Na-CNF full cell remained stable over its 500 cycles and is consistent with Na metal half cells (Figures 6c,f and Figure S15b,c).

To understand the role of the electrodeposited lithium and sodium, full cells were assembled using the pristine CNF as the anode (Figure S16). Both NMC622 and NFM333 cells exhibit poor cyclability with the pristine CNF anode. The NMC622 cell can sustain 24 mAh g⁻¹ capacity during its cycle life. The NFM cell initially has 20 mAh g⁻¹ and quickly fades to 5 mAh g⁻¹. When these cathodes are paired with a graphite or hard carbon anode, reasonable cell capacity can be obtained. Collectively, these results suggest that the pre-lithiation and pre-sodiation of the CNF through electrodeposition directly contribute to the battery performance of the composite anodes in full cells.

Conclusion

Through using a semi-crystalline CNF material, we have demonstrated the fundamental effect that the structural characteristics of the CNF has on the intercalation, electrodeposition, and cycling behavior between lithium/sodium metal and the CNF host. Sodium metal has been shown to plate uniformly throughout the CNF host material, and lithium metal is unable to coat the CNF and instead forms a heterogenous distribution of metal clusters along the CNF surface. However, the instability of the electrodeposited sodium metal causes the Na-CNF to undergo change in its primary cycling mechanism from metal stripping/plating to sodium ion intercalation/de-intercalation. The (de)intercalation mechanism enables Na-CNF to sustain 2,000 hours of symmetric cycling with no significant increase in overpotential or impedance and to retain 75% and 80% capacity retention at 1C and 2C after 500 full cell cycles, respectively. The

electrodeposited lithium metal has better cyclability and lower overpotential, but the inability to intercalate into the CNF crystal structure limits the effectiveness of the composite anode. Li-CNF can only sustain 160 hours of stable symmetric cell cycling, and 140 and 160 full cell cycles at 1C and 2C, respectively, before undergoing active material depletion and suffering from significant polarization. The semi-crystalline carbon structure with a d_{002} of 3.59 Å accommodates reversible intercalation/de-intercalation and adsorption for Na ions, allowing for long-term, stable performance for Na-CNF. However, Li ion interaction is primarily limited to surface adsorption. The CNF host may act as a “scavenger” to protect the intercalated Na ions from being consumed by side reactions with the electrolyte, allowing for the enhanced stability to enable stable, long term cycling. Through our characterization analysis, we can conclude that the surface functionalization and ability to adsorb and/or intercalate is a crucial aspect in the -philic or -phobic relationship between the alkali metal and the substrate. The optimization parameters of the carbon substrate’s crystallinity to improve the ionic and metal-host interaction will differ for lithium and sodium. This study will help guide the direction for improved alkali composite anode designs *via* crystalline structure optimization of the carbon host material.

Acknowledgements

This work is primarily supported by the Institute for Critical Technology and Applied Science at Virginia Tech. The Na cathode was developed based on a project funded by the National Science Foundation (No. CBET-1912885). The Li cathode was developed based on a project funded by the National Science Foundation (No. DMR-1832613). This work was performed in part at the Surface Analysis Laboratory in Department of Chemistry at Virginia Tech, which is supported by the National Science Foundation under Grant No. CHE-1531834. The authors thank Dr. Xu Feng for the technical assistance in XPS measurements.

Authors contribution

F.L. led the project. D.J.K. and F.L. designed the experiments. D.J.K. performed SEM imaging, XPS analysis and electrochemical measurements. L.T. and Z.Z. synthesized the CNF. L.M. synthesized the cathode precursor materials. M.M.R conducted the XRD measurements. C.K.

performed TEM imaging. L.T. and L.M. participated in the data discussion. D.J.K. and F.L. analyzed the data and wrote the manuscript with the help of all coauthors.

Conflict of Interest

The authors declare no conflict of interest.

References:

- (1) Albertus, P. Babinec, S. Litzelman, S. Newman, A. Status and Challenges in Enabling the Lithium Metal Electrode for High-Energy and Low-Cost Rechargeable Batteries. *Nat. Energy* 2018, 3, 16–21.
- (2) Lin, D. Liu, Y. Cui, Y. Reviving the Lithium Metal Anode for High-Energy Batteries. *Nat. Nanotechnol.* 2017, 12 (3), 194–206.
- (3) Guo, Y. Li, H. Zhai, T. Reviving Lithium-Metal Anodes for Next-Generation High-Energy Batteries. *Adv. Mater.* 2017, 29 (29), 1700007.
- (4) Manthiram, A. Knight, J. C. Myung, S. T. Oh, S. M. Sun, Y. K. Nickel-Rich and Lithium-Rich Layered Oxide Cathodes: Progress and Perspectives. *Adv. Energy Mater.* 2016, 6 (1), 1501010.
- (5) Myung, S. T. Maglia, F. Park, K. J. Yoon, C. S. Lamp, P. Kim, S. J. Sun, Y. K. Nickel-Rich Layered Cathode Materials for Automotive Lithium-Ion Batteries: Achievements and Perspectives. *ACS Energy Lett.* 2017, 2 (1), 196–223.
- (6) Qian, Y. Hu, S. Zou, X. Deng, Z. Xu, Y. Cao, Z. Kang, Y. Deng, Y. Shi, Q. Xu, K. Deng, Y. How Electrolyte Additives Work in Li-Ion Batteries. *Energy Storage Mater.* 2019, 20, 208–215.
- (7) Zhang, X. Q. Cheng, X. B. Chen, X. Yan, C. Zhang, Q. Fluoroethylene Carbonate Additives to Render Uniform Li Deposits in Lithium Metal Batteries. *Adv. Funct. Mater.* 2017, 27 (10), 1605989.
- (8) Liu, Q. Q. Petibon, R. Du, C. Y. Dahn, J. R. Effects of Electrolyte Additives and Solvents on Unwanted Lithium Plating in Lithium-Ion Cells. *J. Electrochem. Soc.* 2017, 164 (6),

1173–1183.

- (9) Li, N. W. Yin, Y. X. Yang, C. P. Guo, Y. G. An Artificial Solid Electrolyte Interphase Layer for Stable Lithium Metal Anodes. *Adv. Mater.* 2016, 28 (9), 1853–1858.
- (10) Wang, Y. Li, P. Dong, X. Li, C. Liu, J. Liu, Y. Feng, W. Wang, C. Xia, Y. Anchoring Artificial Solid Electrolyte Interphase Layer on 3D Current Collector for High-Performance Lithium Anode. *Angew. Chemie Int. Ed.* 2019, 7 (58), 2093-2097
- (11) Park, J. Jeong, J. Lee, Y. Oh, M. Ryou, M. H. Lee, Y. M. Micro-Patterned Lithium Metal Anodes with Suppressed Dendrite Formation for Post Lithium-Ion Batteries. *Adv. Mater. Interfaces* 2016, 3 (11), 1600140.
- (12) Kim, S. Choi, J. Lee, H. Jeong, Y. C. Lee, Y. M. Ryou, M. H. Suppression of Dendrites and Granules in Surface-Patterned Li Metal Anodes Using CsPF₆. *J. Power Sources* 2019, 413 (2018), 344–350.
- (13) Park, J. Kim, D. Jin, D. Phatak, C. Cho, K. Y. Lee, Y. G. Hong, S. Ryou, M. H. Lee, Y. M. Size Effects of Micro-Pattern on Lithium Metal Surface on the Electrochemical Performance of Lithium Metal Secondary Batteries. *J. Power Sources* 2018, 408, 136–142.
- (14) Kautz, D. J. Mu, L. Tao, L. Lin, F. Zheng, Z. Nordlund, D. Feng, X. Understanding the Critical Chemistry to Inhibit Lithium Consumption in Lean Lithium Metal Composite Anodes. *J. Mater. Chem. A* 2018, 6 (33), 16003–16011.
- (15) Huang, Y. Duan, J. Zheng, X. Wen, J. Dai, Y. Wang, Z. Luo, W. Huang, Y. Lithium Metal-Based Composite: An Emerging Material for Next-Generation Batteries. *Matter.* 2020, 3 (4), 1009–1030.
- (16) Huang, G. Han, J. Zhang, F. Wang, Z. Kashani, H. Watanabe, K. Chen, M. Lithiophilic 3D Nanoporous Nitrogen-Doped Graphene for Dendrite-Free and Ultrahigh-Rate Lithium-Metal Anodes. *Adv. Mater.* 2019, 31 (2), 1805334.
- (17) Chen, X. Chen, X. Hou, T. Li, B. Cheng, X. Zhang, R. Zhang, Q. Lithiophilicity Chemistry of Heteroatom-Doped Carbon to Guide Uniform Lithium Nucleation in Lithium Metal Anodes. *Sci. Adv.* 2019, 5 (2), eaau7728.

- (18) Tao, L. Xu, Z. Kuai, C. Zheng, X. Wall, C. E. Jiang, C. Esker, A. R. Zheng, Z. Lin, F. Flexible Lignin Carbon Membranes with Surface Ozonolysis to Host Lean Lithium Metal Anodes for Nickel-Rich Layered Oxide Batteries. *Energy Storage Mater.* 2020, 24, 129–137.
- (19) Yue, X. Y. Li, X. L. Wang, W. W. Chen, D. Qiu, Q. Q. Wang, Q. C. Wu, X. J. Fu, Z. W. Shadike, Z. Yang, X. Q. Zhou, Y. N. Wettable Carbon Felt Framework for High Loading Li-Metal Composite Anode. *Nano Energy* 2019, 60 (March), 257–266.
- (20) Zhang, H. Liao, X. Guan, Y. Xiang, Y. Li, M. Zhang, W. Zhu, X. Lithiophilic / Lithiophobic Gradient Interfacial Layer for Highly Stable Lithium Metal Anode. *Nat. Commun.* 2018, 9, 3729.
- (21) Yi, J. Chen, J. Yang, Z. Dai, Y. Li, W. Cui, J. Ciucci, F. Lu, Z. Yang, C. Facile Patterning of Laser-Induced Graphene with Tailored Li Nucleation Kinetics for Stable Lithium-Metal Batteries. *Adv. Energy Mater.* 2019, 9 (38), 1901796.
- (22) Liang, Z. Lin, D. Zhao, J. Lu, Z. Liu, Y. Liu, C. Lu, Y. Wang, H. Yan, K. Tao, X. Cui, Y. Composite Lithium Metal Anode by Melt Infusion of Lithium into a 3D Conducting Scaffold with Lithiophilic Coating. *Proc. Natl. Acad. Sci. U. S. A.* 2016, 113 (11), 2862–2867.
- (23) Lin, D. Liu, Y. Liang, Z. Lee, H.-W. Sun, J. Wang, H. Yan, K. Xie, J. Cui, Y. Layered Reduced Graphene Oxide with Nanoscale Interlayer Gaps as a Stable Host for Lithium Metal Anodes. *Nat. Nanotechnol.* 2016, 11, 626–632.
- (24) Yu, B. Tao, T. Mateti, S. Lu, S. Chen, Y. Nanoflake Arrays of Lithiophilic Metal Oxides for the Ultra-Stable Anodes of Lithium-Metal Batteries. *Adv. Funct. Mater.* 2018, 28 (36), 1803023.
- (25) Slater, M. D. Kim, D. Lee, E. Johnson, C. S. Sodium-Ion Batteries. *Adv. Funct. Mater.* 2013, 23 (8), 947–958.
- (26) Liu, Y. Merinov, B. V. Goddard, W. A. Origin of Low Sodium Capacity in Graphite and Generally Weak Substrate Binding of Na and Mg among Alkali and Alkaline Earth Metals. *Proc. Natl. Acad. Sci.* 2016, 113 (14), 3735–3739.

- (27) Li, Y. Lu, Y. Adelhelm, P. Titirici, M. M. Hu, Y. S. Intercalation Chemistry of Graphite: Alkali Metal Ions and Beyond. *Chem. Soc. Rev.* 2019, 48 (17), 4655–4687.
- (28) Xu, Z.-L. Yoon, G. Park, K.-Y. Park, H. Tamwattana, O. Joo Kim, S. Seong, W. M. Kang, K. Tailoring Sodium Intercalation in Graphite for High Energy and Power Sodium Ion Batteries. *Nat. Commun.* 2019, 10 (1), 2598.
- (29) Sun, N. Guan, Z. Liu, Y. Cao, Y. Zhu, Q. Liu, H. Wang, Z. Zhang, P. Xu, B. Extended “Adsorption–Insertion” Model: A New Insight into the Sodium Storage Mechanism of Hard Carbons. *Adv. Energy Mater.* 2019, 9 (32), 1901351.
- (30) Stevens, D. A. Dahn, J. R. High Capacity Anode Materials for Rechargeable Sodium-Ion Batteries. *J. Electrochem. Soc.* 2002, 147 (4), 1271.
- (31) Matei Ghimbeu, C. Górká, J. Simone, V. Simonin, L. Martinet, S. Vix-Guterl, C. Insights on the Na⁺ion Storage Mechanism in Hard Carbon: Discrimination between the Porosity, Surface Functional Groups and Defects. *Nano Energy* 2018, 44, 327–335.
- (32) Dou, X. Hasa, I. Saurel, D. Vaalma, C. Wu, L. Buchholz, D. Bresser, D. Komaba, S. Passerini, S. Hard Carbons for Sodium-Ion Batteries : Structure , Analysis , Sustainability , and Electrochemistry. *Mater. Today* 2019, 23, 87–104.
- (33) Li, Y. Yuan, Y. Bai, Y. Liu, Y. Wang, Z. Li, L. Wu, F. Amine, K. Wu, C. Lu, J. Insights into the Na + Storage Mechanism of Phosphorus-Functionalized Hard Carbon as Ultrahigh Capacity Anodes. *Adv. Energy Mater.* 2018, 8 (18), 1702781.
- (34) Bommier, C. Mitlin, D. Ji, X. Internal Structure – Na Storage Mechanisms – Electrochemical Performance Relations in Carbons. *Prog. Mater. Sci.* 2018, 97 (April), 170–203.
- (35) Luo, W. Zhang, Y. Xu, S. Dai, J. Hitz, E. Li, Y. Yang, C. Chen, C. Liu, B. Hu, L. Encapsulation of Metallic Na in an Electrically Conductive Host with Porous Channels as a Highly Stable Na Metal Anode. *Nano Lett.* 2017, 17 (6), 3792–3797.
- (36) Ye, H. Wang, C. Y. Zuo, T. T. Wang, P. F. Yin, Y. X. Zheng, Z. J. Wang, P. Cheng, J. Cao, F. F. Guo, Y. G. Realizing a Highly Stable Sodium Battery with Dendrite-Free Sodium Metal Composite Anodes and O3-Type Cathodes. *Nano Energy* 2018, 48, 369–

376.

- (37) Go, W. Kim, M. Park, J. Lim, C. H. Joo, S. H. Kim, Y. Lee, H.-W. Nanocrevasse-Rich Carbon Fibers for Stable Lithium and Sodium Metal Anodes. *Nano Lett.* 2018, 19 (3), 1504–1511.
- (38) Jia, R. Chen, J. Zhao, J. Zheng, J. Song, C. Li, L. Zhu, Z. Synthesis of Highly Nitrogen-Doped Hollow Carbon Nanoparticles and Their Excellent Electrocatalytic Properties in Dye-Sensitized Solar Cells. *J. Mater. Chem.* 2010, 20 (48), 10829–10834.
- (39) Zhang, B. Ghimbeu, C. M. Laberty, C. Vix-Guterl, C. Tarascon, J. M. Correlation between Microstructure and Na Storage Behavior in Hard Carbon. *Adv. Energy Mater.* 2016, 6 (1), 1501558.
- (40) Yoon, H. J. Kim, N. R. Jin, H. J. Yun, Y. S. Macroporous Catalytic Carbon Nanotemplates for Sodium Metal Anodes. *Adv. Energy Mater.* 2018, 8 (6), 1701261.
- (41) Zuo, T.-T. Wu, X.-W. Yang, C.-P. Yin, Y.-X. Ye, H. Li, N.-W. Guo, Y.-G. Graphitized Carbon Fibers as Multifunctional 3D Current Collectors for High Areal Capacity Li Anodes. *Adv. Mater.* 2017, 29 (29), 1700389.
- (42) Ji, K. Han, J. Hirata, A. Fujita, T. Shen, Y. Ning, S. Liu, P. Kashani, H. Tian, Y. Ito, Y. Fujita, J. ichi Oyama, Y. Lithium Intercalation into Bilayer Graphene. *Nat. Commun.* 2019, 10 (1), 275.
- (43) Hooley, J. G. Physical Chemistry and Mechanism of Intercalation in Graphite. *Mater. Sci. Eng.* 1977, 31 (C), 17–24.
- (44) Komaba, S. Murata, W. Ishikawa, T. Yabuuchi, N. Ozeki, T. Nakayama, T. Ogata, A. Gotoh, K. Fujiwara, K. Electrochemical Na Insertion and Solid Electrolyte Interphase for Hard-Carbon Electrodes and Application to Na-Ion Batteries. *Adv. Funct. Mater.* 2011, 21 (20), 3859–3867.
- (45) Qiu, S. Xiao, L. Sushko, M. L. Han, K. S. Shao, Y. Yan, M. Liang, X. Mai, L. Feng, J. Cao, Y. Ai, X. Yang, H. Liu, J. Manipulating Adsorption–Insertion Mechanisms in Nanostructured Carbon Materials for High-Efficiency Sodium Ion Storage. *Adv. Energy Mater.* 2017, 7 (17), 1700403.

- (46) Yang, G. Li, Y. Tong, Y. Qiu, J. Liu, S. Zhang, S. Guan, Z. Xu, B. Wang, Z. Chen, L. Lithium Plating and Stripping on Carbon Nanotube Sponge. *Nano Lett.* 2019, *19* (1), 494–499.
- (47) Ko, J. Yoon, Y. S. Recent Progress in LiF Materials for Safe Lithium Metal Anode of Rechargeable Batteries: Is LiF the Key to Commercializing Li Metal Batteries? *Ceramics International*. 2019, *45* (1), 30-49.
- (48) Xie, J. Liao, L. Gong, Y. Li, Y. Shi, F. Pei, A. Sun, J. Zhang, R. Kong, B. Subbaraman, R. Christensen, J. Cui, Y. Stitching H-BN by Atomic Layer Deposition of LiF as a Stable Interface for Lithium Metal Anode. *Sci. Adv.* 2017, *3* (11), eaao3170.
- (49) Michan, A. L. Parimalam, B. S. Leskes, M. Kerber, R. N. Yoon, T. Grey, C. P. Lucht, B. L. Fluoroethylene Carbonate and Vinylene Carbonate Reduction: Understanding Lithium-Ion Battery Electrolyte Additives and Solid Electrolyte Interphase Formation. *Chem. Mater.* 2016, *28* (22), 8149–8159.
- (50) Günter, F. J. Habedank, J. B. Schreiner, D. Neuwirth, T. Gilles, R. Reinhart, G. Introduction to Electrochemical Impedance Spectroscopy as a Measurement Method for the Wetting Degree of Lithium-Ion Cells. *J. Electrochem. Soc.* 2018, *165* (14), A3249–A3256.
- (51) Cohen, Y. S. Cohen, Y. Aurbach, D. Micromorphological Studies of Lithium Electrodes in Alkyl Carbonate Solutions Using in Situ Atomic Force Microscopy. *J. Phys. Chem. B* 2000, *104* (51), 12282–12291.
- (52) Tikekar, M. D. Choudhury, S. Tu, Z. Archer, L. A. Design Principles for Electrolytes and Interfaces for Stable Lithium-Metal Batteries. *Nat. Energy* 2016, *1* (9), 16114.
- (53) Kim, J. D. Roh, J.-S. Kim, M.-S. Effect of Carbonization Temperature on Crystalline Structure and Properties of Isotropic Pitch-Based Carbon Fiber. *Carbon Lett.* 2017, *21*, 51–60.
- (54) Feng, Y. Tao, L. He, Y. Jin, Q. Zheng, Y. Kuai, C. Li, M. Hou, Q. Zheng, Z. Lin, F. Huang, H. Chemical-Enzymatic Fractionation to Unlock the Potential of Biomass-Derived Carbon Materials for Sodium Ion Batteries. *J. Mater. Chem. A* 2019, 26954–26965.

- (55) Stevens, D. A. Dahn, J. R. The Mechanisms of Lithium and Sodium Insertion in Carbon Materials. *J. Electrochem. Soc.* 2002, *148* (8), A803.
- (56) Wang, H. Liao, X.-Z. Yang, Y. Yan, X. He, Y.-S. Ma, Z.-F. Large-Scale Synthesis of $\text{NaNi}_{1/3}\text{Fe}_{1/3}\text{Mn}_{1/3}\text{O}_2$ as High Performance Cathode Materials for Sodium Ion Batteries. *J. Electrochem. Soc.* 2016, *163* (3), A565–A570.
- (57) Mu, L. Feng, X. Kou, R. Zhang, Y. Guo, H. Tian, C. Sun, C.-J. Du, X.-W. Nordlund, D. Xin, H. L. Lin, F. Deciphering the Cathode–Electrolyte Interfacial Chemistry in Sodium Layered Cathode Materials. *Adv. Energy Mater.* 2018, *8* (34), 1801975.
- (58) Mu, L. Rahman, M. M. Zhang, Y. Feng, X. Du, X. W. Nordlund, D. Lin, F. Surface Transformation by a “Cocktail” Solvent Enables Stable Cathode Materials for Sodium Ion Batteries. *J. Mater. Chem. A* 2018, *6* (6), 2758–2766.
- (59) Xu, J. Lin, F. Doeff, M. M. Tong, W. A Review of Ni-Based Layered Oxides for Rechargeable Li-Ion Batteries. *J. Mater. Chem. A* 2017; , 874–901.

Supplemental Information

Investigating “Lean” Electrodeposited Lithium and Sodium Metal for Hybrid Ion/Metal Carbon Composite Anodes

*David J. Kautz, Lei Tao, Linqin Mu, Muhammad Mominur Rahman, Chunguang Kuai, Zhifeng Zheng, and Feng Lin **

D. J. Kautz, Dr. L. Tao, Dr. L. Mu, M. M. Rahman, Dr. C. Kuai, Prof. F. Lin

Department of Chemistry, Virginia Tech, Blacksburg, VA 24061, USA

Email: fenglin@vt.edu

Prof. Z. Zheng

Fujian Engineering and Research Center of Clean and High-valued Technologies for Biomass,

College of Energy, Xiamen University, Xiamen 361102, China

Experimental Section

Materials

For the carbon nanofiber preparation, walnut shell (*Juglans Sigillata*) was ground (>100 mesh) and dried in an oven at 80 °C. The mixture of walnut shell powder, phenol and sulfuric acid (concentrated 98%) at a mass ratio of 1:4:0.03 was liquefied for 2 hours at 150 °C. Subsequently, the mixture was poured into dioxane/water (8/2, v/v) at a volume ratio of 1/15. The diluted solution was altered and concentrated under reduced pressure to obtain impurity-free liquefied products. The liquefied phenol formaldehyde resin (LPF) was synthesized by formaldehyde (F) and liquefied products (LP) with sodium hydroxide (NaOH) as a catalyst (molar (LPF), LP, NaOH solution and 80% of the total F were added into ratio, $F/LP = 1.45/1$, $NaOH/LP = 0.2/1$). In synthesizing resin (LPF), LP, NaOH, and 80% of the total F were added into a three-neck flask. The solution was heated to 82 °C for 60 min. After, the remaining 20% of F was added. The reaction temperature was increased to and kept at 87 °C and stirring for 120 min. The solution was cooled to room temperature. Subsequently, the synthesized LPF was diluted to 18 wt% in solid content with distilled water and 12 wt% polyvinyl alcohol (PVA) aqueous solution added to the LPF to adjust the electro-spinability (mass ratio of LPF/PVA $\frac{1}{4}$ 8/2). The mixed solution stirring was continued for 2 h. Electrospun nanofibers were prepared using an electrospinning device (ET-2535H, Ucalery), which consisted of a high voltage power supply, a syringe pump, and a roller (covered with aluminum foil) connected to the negative pole for collecting the fibers. The spinning solution was loaded into a 5 mL plastic syringe with a 22-gauge needle connected to the positive pole of a voltage generator. During spinning, the distance was adjusted to 25 cm between the tip of needle and the roller, an operating voltage was ranged from 16 kV and the feeding rate of spin was

maintained at 0.05 mL min^{-1} . The carbon nanofibers were fabricated by one-step carbonation at $1800 \text{ }^{\circ}\text{C}$ at a rate of $5^{\circ}\text{C min}^{-1}$ and held for 60 min in a nitrogen atmosphere.

The $\text{LiNi}_{0.6}\text{Mn}_{0.2}\text{Co}_{0.2}\text{O}_2$ cathode materials were synthesized using a co-precipitation method followed by calcination. The acid metal solution was prepared using $0.6 \text{ M NiSO}_4 \cdot 6\text{H}_2\text{O}$ (Sigma Aldrich, 99.99%), $0.2 \text{ M MnSO}_4 \cdot \text{H}_2\text{O}$ (Sigma Aldrich, 99%) and $0.2 \text{ M CoSO}_4 \cdot 7\text{H}_2\text{O}$ (Sigma Aldrich, 99%) as the raw materials dissolved in $100 \text{ mL H}_2\text{O}$. The transition metal solution, starting solution (40 mL NaOH and $\text{NH}_3 \cdot \text{H}_2\text{O}$ aqueous solution with a molar ratio $\text{NaOH}/\text{NH}_3 = 1.2$, with the pH value was adjusted to 10.5) and base solution (100 mL NaOH and $\text{NH}_3 \cdot \text{H}_2\text{O}$ aqueous solution with a molar ratio $\text{NaOH}/\text{NH}_3 = 1.2$) were made and separately stored under N_2 protection. The transition metal solution and base solution were simultaneously pumped into the starting solution at a drop rate of 2 mL min^{-1} with continuously stirring at $50 \text{ }^{\circ}\text{C}$ under the N_2 protection. The drop rate of the base solution was frequently tuned to keep the pH at 10.5 ± 0.2 . The precipitate was collected, washed and filtered with DI water and dried in a vacuum oven overnight at $100 \text{ }^{\circ}\text{C}$. The dried precursor was then mixed with LiOH thoroughly and calcined under air flow (2 L min^{-1}) at $725 \text{ }^{\circ}\text{C}$ for 6 hours.

The $\text{NaNi}_{0.33}\text{Fe}_{0.3}\text{Mn}_{0.33}\text{Ti}_{0.04}\text{O}_2$ cathode materials were synthesized using a co-precipitation method followed by calcination. Two separate acidic metal solutions were prepared. First, the acidic metal sulfate solutions were prepared using $0.033 \text{ M NiSO}_4 \cdot 6\text{H}_2\text{O}$ (Sigma Aldrich, 99.99%), $0.030 \text{ M FeSO}_4 \cdot 7\text{H}_2\text{O}$ (Sigma Aldrich, 98%), and $0.033 \text{ M MnSO}_4 \cdot \text{H}_2\text{O}$ (Sigma Aldrich, 99%) as the raw materials dissolved in $100 \text{ mL H}_2\text{O}$. The other acidic solution consisted of 0.004 M TiOSO_4 dissolved in 100 mL water . The starting solution (40 mL NaOH and pH value adjusted to 10.5 using sulfuric acid) and base solution ($100 \text{ mL NaOH}/\text{NH}_3 \cdot \text{H}_2\text{O}$ aqueous solution with a molar ratio of $\text{NaOH}/\text{NH}_3 = 2.4$ (0.2 m NaOH)). The transition metal solution and base solution

were simultaneously pumped into the starting solution at a drop rate of 2 mL min⁻¹ with continuously stirring at 55 °C under N₂ protection. The acid TiOSO₄ solution was pumped into the acidic NiSO₄/FeSO₄/MnSO₄ solution at a rate of ≈1 mL min⁻¹. The drop rate of the base solution was frequently tuned to keep the pH at 10.5 ± 0.2. The precipitate was collected, washed and filtered with DI water and dried in a vacuum oven overnight at 100 °C. The dried precursor was then thoroughly mixed with nanosized Na₂CO₃ (the molar ratio of TM/Na was 1:1.08), transferred into a box furnace and calcined at 850 °C for 10 h.

Material Characterization

The morphologies of the materials were investigated using a scanning electron microscope (SEM) (LEO FESEM) at an accelerating voltage of 5 kV. TEM images were acquired on a JEOL 2100 TEM operated at 200 keV. N₂ adsorption-desorption was acquired on a Micromeritics-3Flex surface characterization analyzer. The surface area was calculated using a Brunauer-Emmett-Teller (BET) method in the linear range of P/P₀ = 0.01-0.1. XPS characterization was performed on a PHI VersaProbe III scanning XPS microscope using monochromatic Al K-alpha X-ray source (1486.6 eV). Samples were transferred from an Ar-filled glove box to the XPS ultrahigh vacuum chamber via a vacuum transfer vessel. All binding energies were referenced to C-C peak at 284.8 eV. XRD characterization was performed on Rigaku Miniflex II. Electrodes were retrieved inside Ar-filled glovebox and sealed in Kapton tape.

Electrochemical Characterization

The NMC composite electrode was prepared with 90% active material, 5% carbon black, and 5% poly(vinylidene difluoride) (PVDF) binder. The NFM electrode was prepared with 85% active material, 10% carbon black, and 5% PVDF binder. The PVDF solution was prepared with

N-methyl 2-pyrrolidone (NMP) as the solvent. The cathode slurry for NMC and NFM was prepared by mixing the PVDF solution with the respective cathode active material and carbon black powder. The slurry was mixed in a Speedmixer for a set amount of time to ensure a homogeneous mixture. The slurry was casted onto carbon-coated Al foil using the doctor blade casting method at 70 °C. The dried casted electrode was cut to 10 mm diameter electrodes and dried in a vacuum oven overnight at 120 °C. The dried electrodes were stored in an Ar-filled glovebox. Total active material mass loading for both NMC and NFM cathodes was $\sim 4 \text{ mg cm}^{-2}$. 1C was defined as fully charging the cathode in 1 h corresponding to a specific current density of 200 mA g⁻¹ for the NMC and 120 mA g⁻¹ for the NFM cathodes. Metal composite anodes were prepared through electrodeposition. Hard carbon and graphite electrode were prepared by mixing 90% active material with 10% PVDF using NMP as the solvent. The slurry was mixed in a Speedmixer and casted onto copper foil using the doctor blade method and dried at 70 °C. The resulting electrode was cut into 16 mm discs and dried in a vacuum oven overnight for 120 °C and subsequently placed into an Ar-filled glovebox. The metal-CNF composite anode was prepared by adhering a pristine CNF disc (2 cm²) copper current collector as the positive electrode and a lithium or sodium foil disc (2 cm²) as the negative electrode in a coin cell (CR 2032 model). The current density used for electrodeposition was 0.25 mA cm⁻² for a total areal capacity of 3 mAh cm⁻². Graphite and HC composite anodes followed the same electrodeposition procedure as the CNF composite anodes. The NMC and NFM cathodes were combined with the Li/Na-CNF composite anode with glass fiber separator. Lithium cells used 1 M LiPF₆ EC/EMC electrolyte (Gotion, LP57) with 2% VC wt% (Sigma Aldrich, 98%). Sodium cells used 1 M NaPF₆ (98%, Sigma Aldrich) dissolved in a PC solvent (Gotion) with 2% FEC wt% (Sigma Aldrich, 99%). All coin cells were assembled in an Ar-filled glovebox. LANDT battery testers and software was utilized

to collect all full cell, half cell, and symmetric cell cycling data. Cyclic voltammetry measurements were performed on a Princeton Applied Research VersaSTAT 4. Electrochemical impedance spectroscopy measurements were performed on using a Biologic SP-50 potentiostat. All electrochemical coin cell testing was performed at 22 °C.

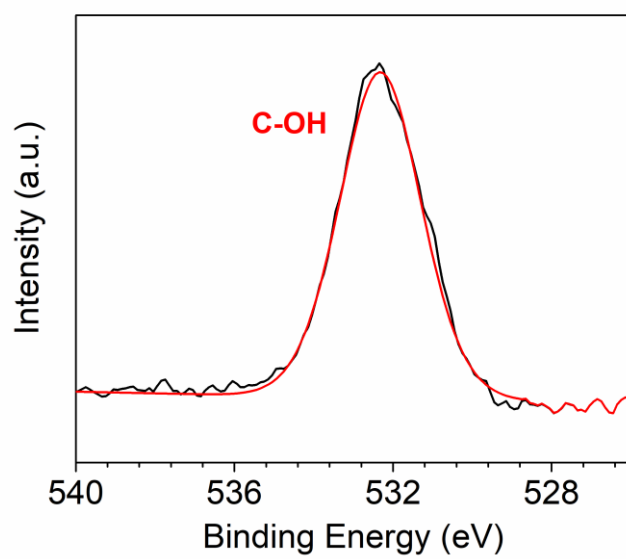


Figure S1) O 1s XPS for pristine carbon nanofiber.

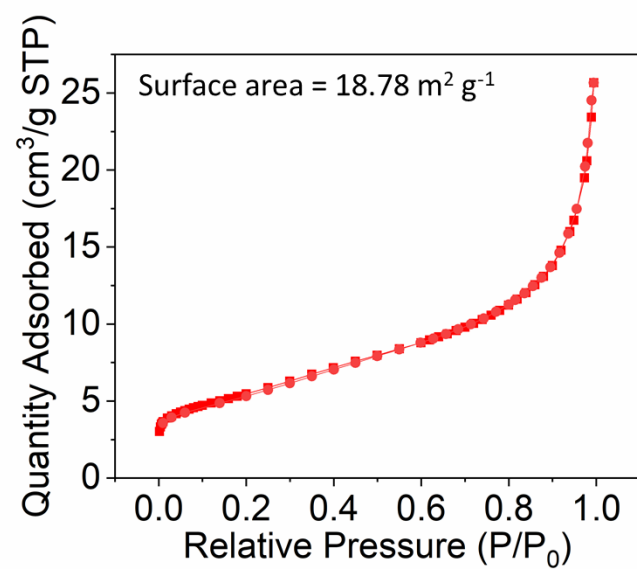


Figure S2) N₂ (77k) adsorption-desorption isotherm for pristine carbon nanofiber.

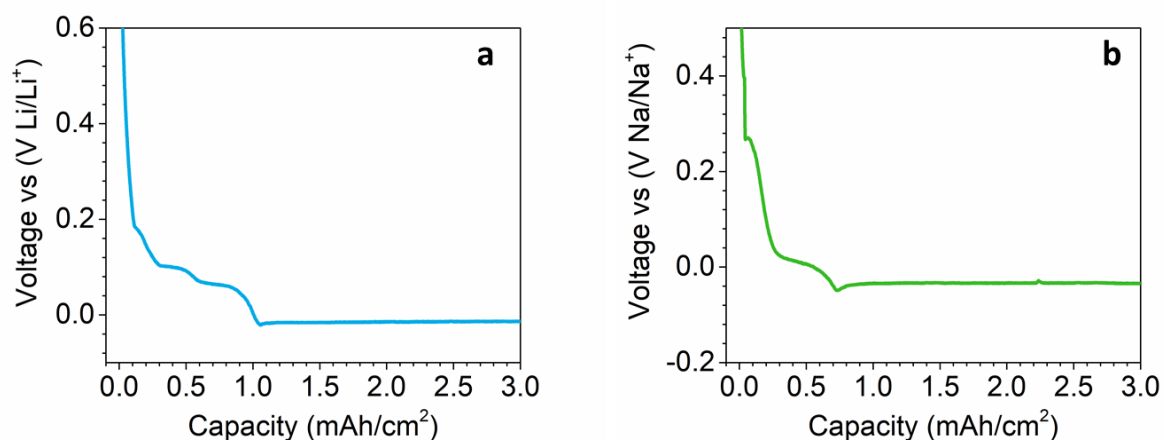


Figure S3) Electrodeposition voltage profiles for a) Li-graphite and b) Na-Hard Carbon composite anodes.

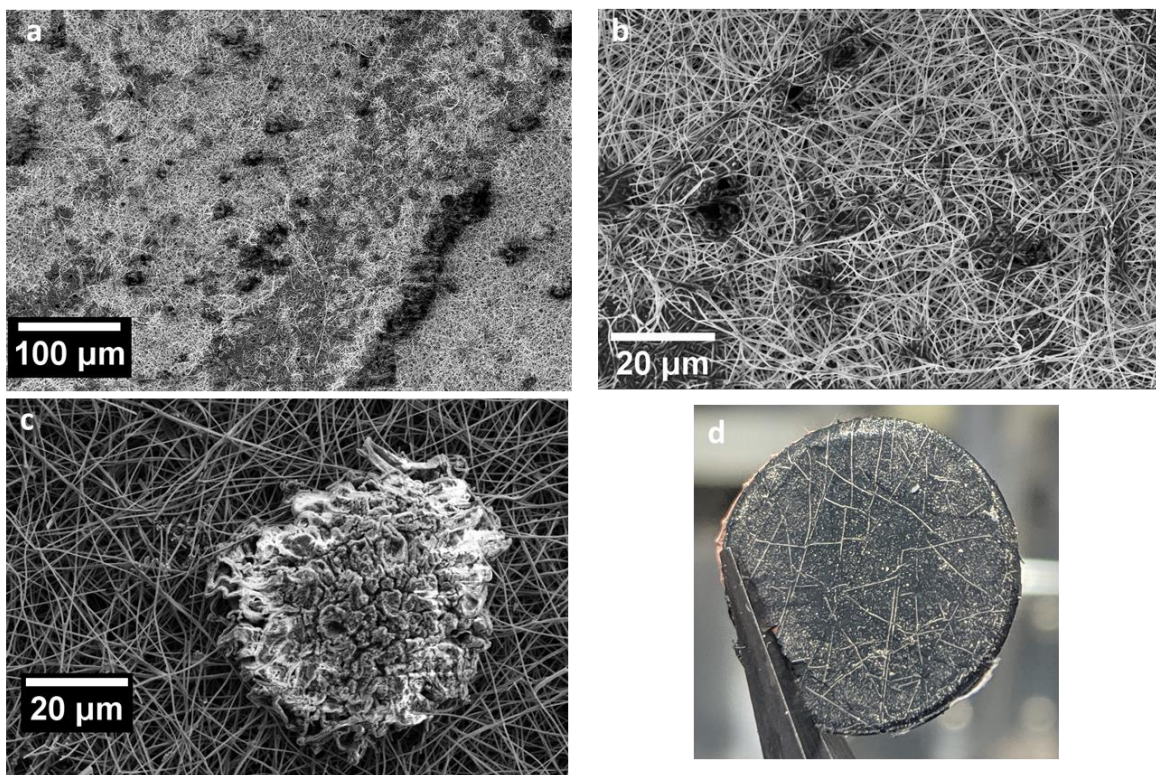


Figure S4) (a-d) Images of Li-CNF after 3 mAh cm^{-2} electrodeposition a) Low magnification SEM image on bottom side of Li-CNF. b) High magnification SEM image on bottom side of Li-CNF. c) High magnification SEM image of large Li metal cluster on top side of Li-CNF and d) photo image of Li-CNF.

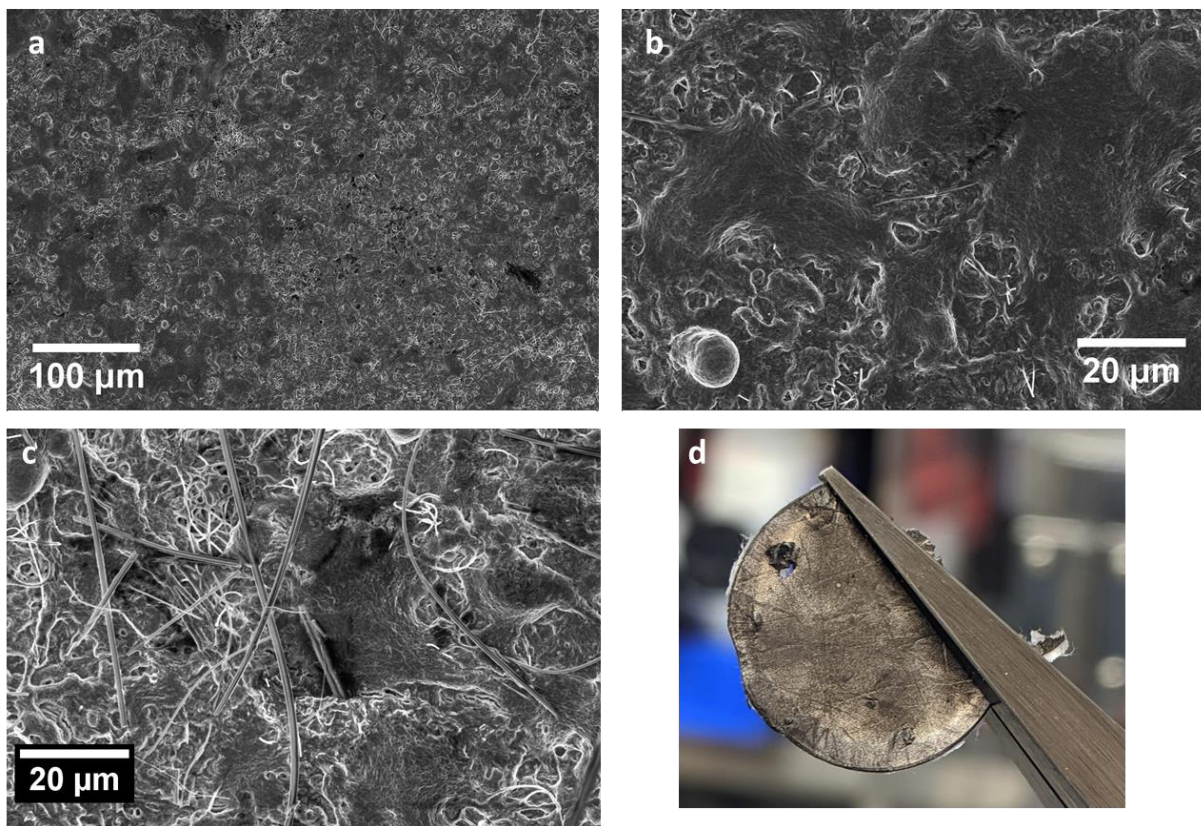


Figure S5) (a-d) Images of Na-CNF after 3 mAh cm⁻² electrodeposition. a) Low magnification SEM image on bottom side of Na-CNF. b) High magnification SEM image on bottom side of Na-CNF. c) High magnification SEM image of large homogeneous plating on top side of Na-CNF. d) Photo image of Na-CNF

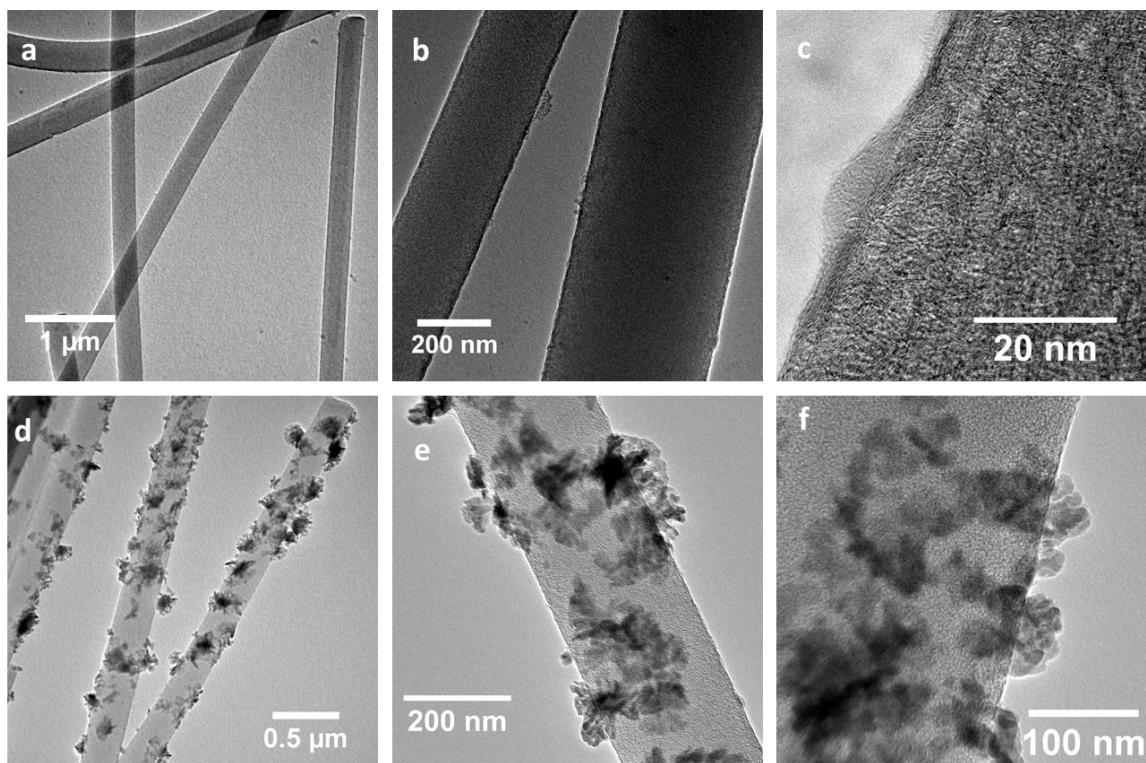


Figure S6) TEM images for Li-CNF (a-c) and Na-CNF(d-f) at varying magnifications.

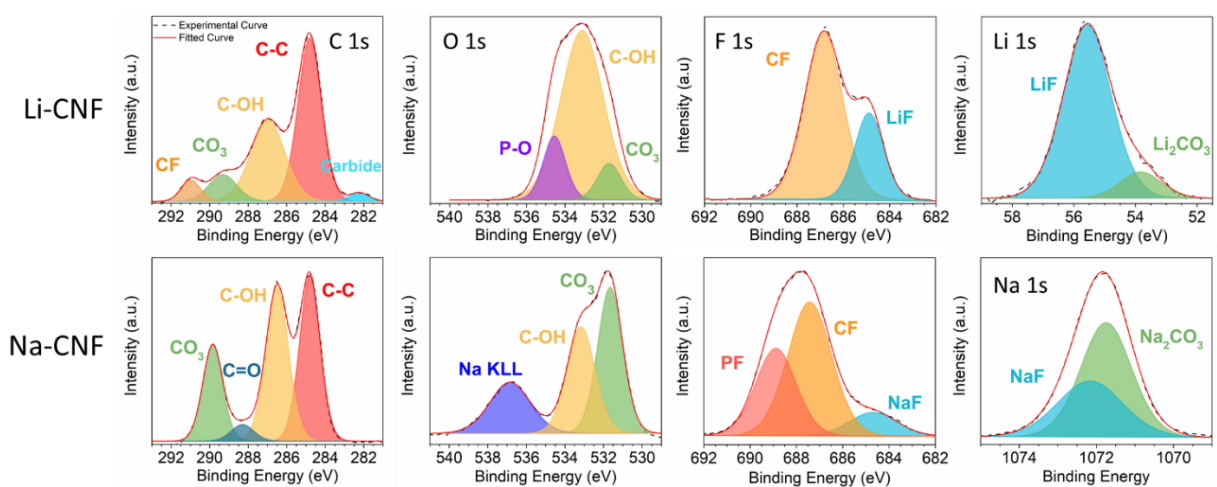


Figure S7) XPS after 3 mAh cm⁻² deposition for Li-CNF C1s, O1s, F1s, Li1s and Na-CNF C1s, O1s, F1s, and Na1s.

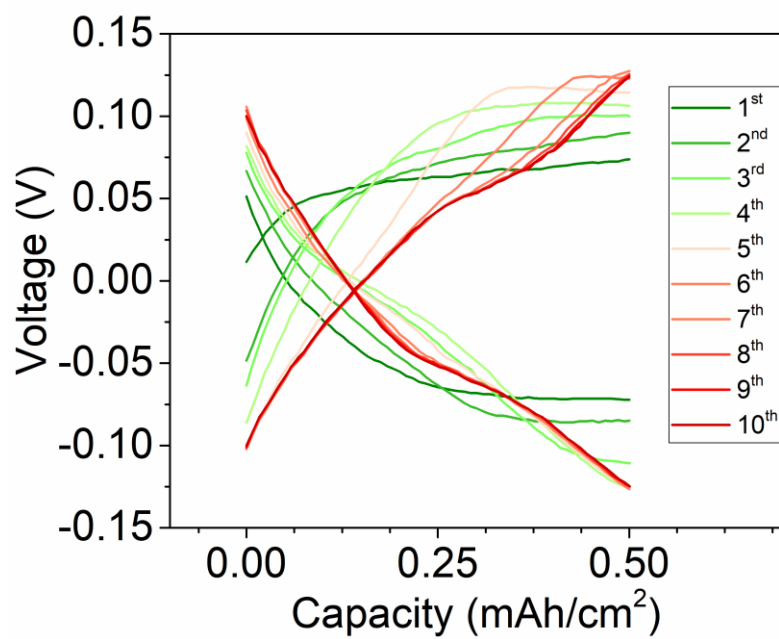


Figure S8) First ten cycles for Na-CNF||Na-CNF symmetric cell demonstrating the change in the cycling mechanism.

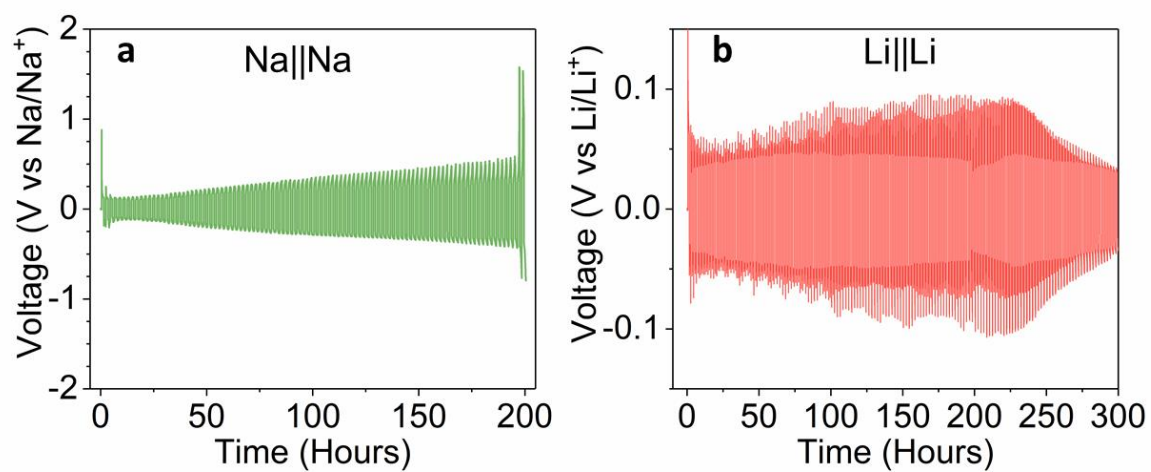


Figure S9) Cycling performance for a) sodium and b) lithium metal symmetric cells.

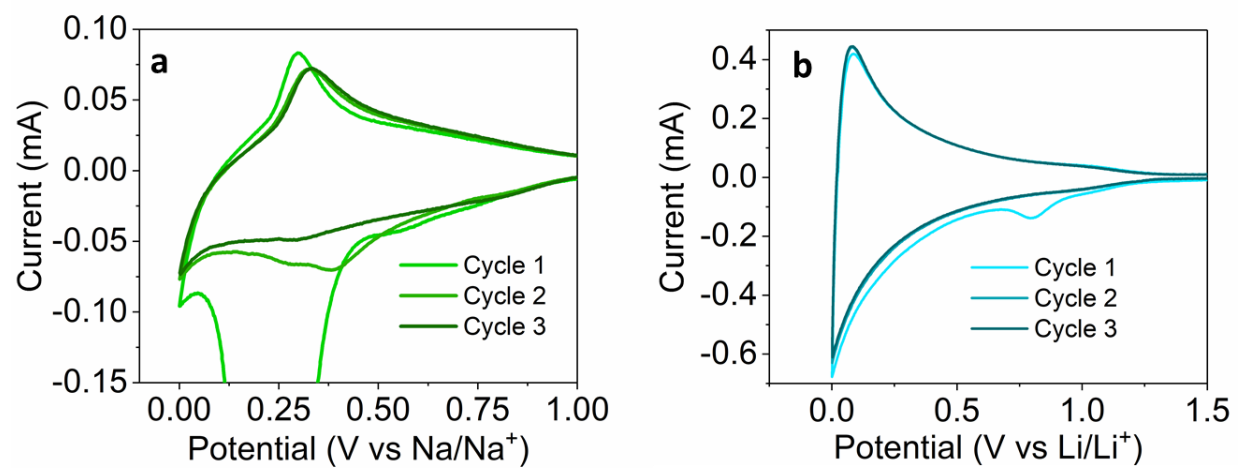


Figure S10) Zoomed in regions for a) Na||CNF and b) Li||CNF for CV cycling.

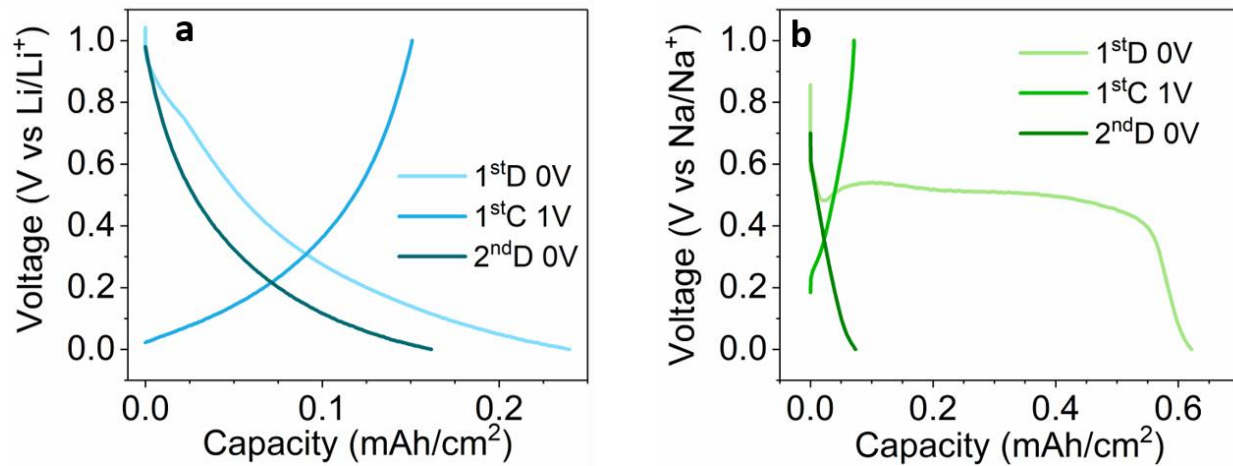


Figure S11) M||CNF half-cell charge (C) and discharge (D) voltage profile of **a)** Na and **b)** Li from 0.01 – 1 V with a current density of 0.05 mA cm⁻²

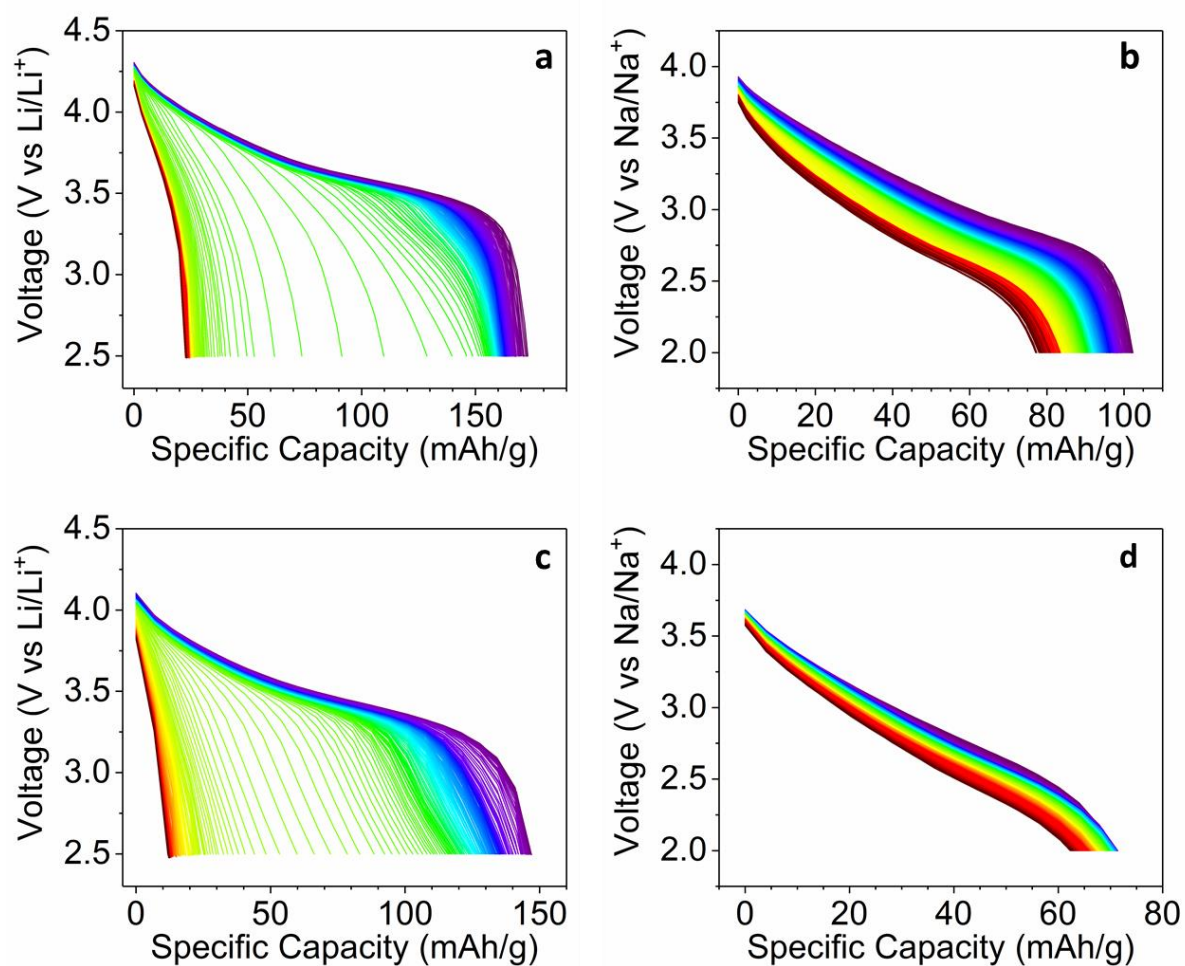


Figure S12) Galvanostatic discharge curves for NMC||Li-CNF and NFM||Na-CNF at 1C (a,b) and 2C (c,d).

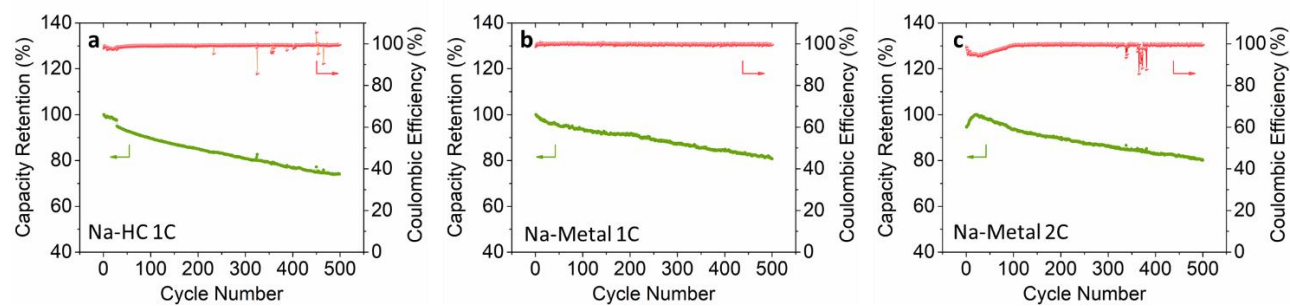


Figure S13) Capacity retention and CE plots for a) Na-HC at 1C, b) Na-Metal at 1C and c) Na-Metal at 2C full and half cells with the NFM333 cathode.

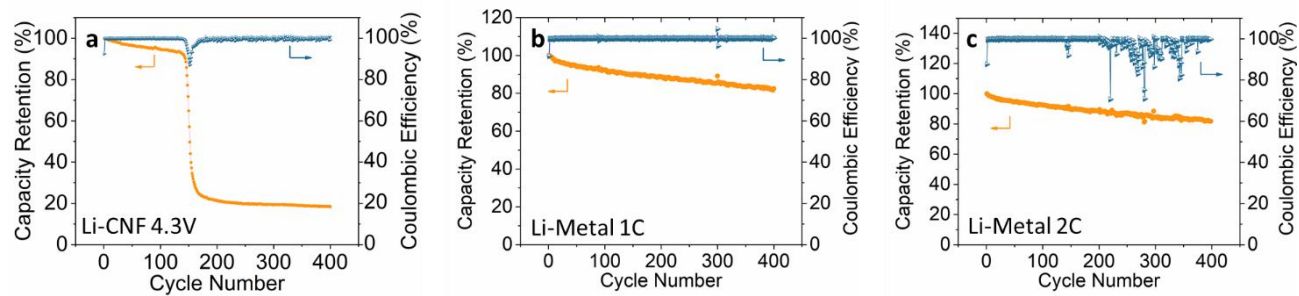


Figure S14) Capacity retention and CE plots for a) Li-CNF with an upper cutoff voltage of 4.3 V at 1C, b) Li-Metal at 1C and c) Li-Metal at 2C full and half cells with the NMC622 cathode.

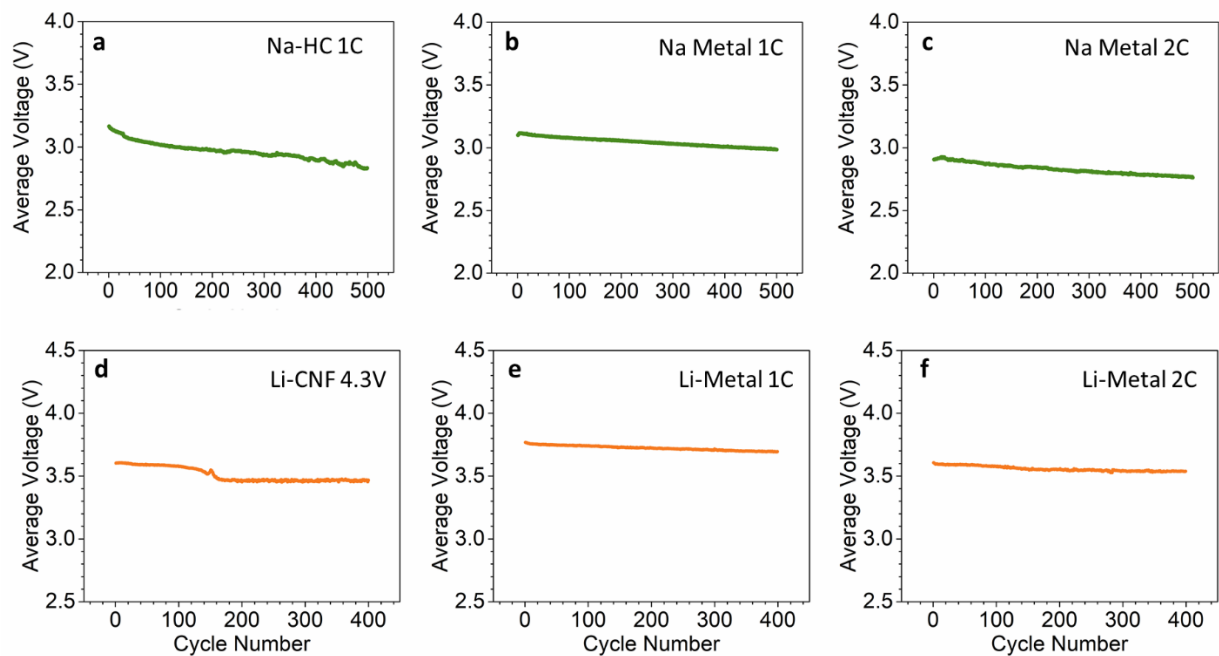


Figure S15) Average voltage profiles for Na- and Li- composite anode full cells and metal anode half cells.

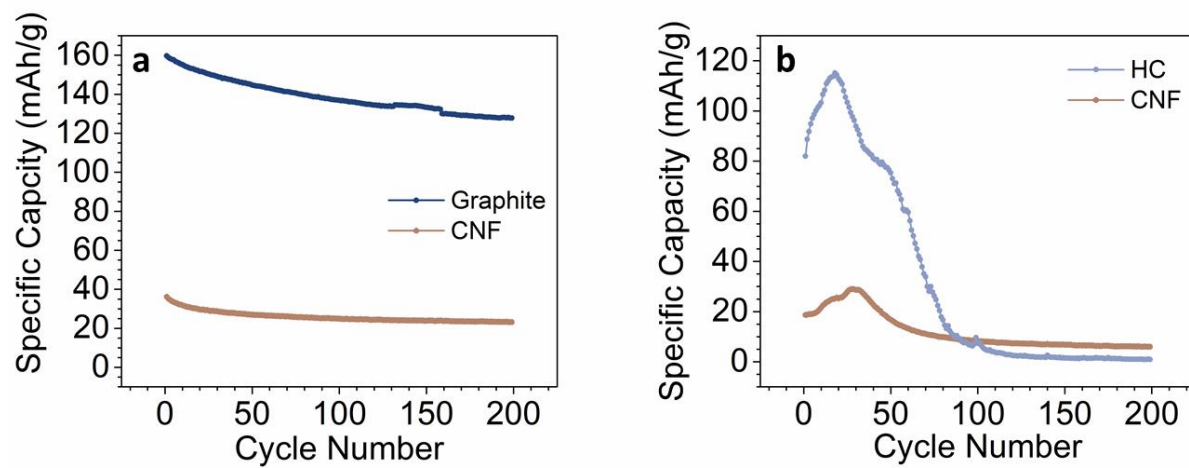


Figure S16) Full cell performance of a) NMC||Graphite and NMC||CNF and b) NFM||HC and NFM||CNF with pristine carbon anodes.